

**BASIC RESEARCH**

# A 1D–0D–3D coupled model for simulating blood flow and transport processes in breast tissue

Marvin Fritz<sup>1</sup>  | Tobias Köppl<sup>1</sup>  | John Tinsley Oden<sup>2</sup> | Andreas Wagner<sup>1</sup>  | Barbara Wohlmuth<sup>1</sup>  | Chengyue Wu<sup>2</sup> 

<sup>1</sup>Department of Mathematics, Technical University of Munich, Garching, Germany

<sup>2</sup>Oden Institute for Computational Engineering and Sciences, The University of Texas at Austin, Austin, Texas, USA

**Correspondence**

Andreas Wagner, Department of Mathematics, Technical University of Munich, Garching, Germany.  
Email: [wagner@ma.tum.de](mailto:wagner@ma.tum.de)

**Funding information**

Deutsche Forschungsgemeinschaft; U.S. Department of Energy, Office of Science, Office of Advanced Scientific Computing Research, Mathematical Multifaceted Integrated Capability Centers, Grant/Award Number: DE-SC0019303; Cancer Prevention and Research Institute of Texas, Grant/Award Number: RR160005

**Abstract**

In this work, we present mixed dimensional models for simulating blood flow and transport processes in breast tissue and the vascular tree supplying it. These processes are considered, to start from the aortic inlet to the capillaries and tissue of the breast. Large variations in biophysical properties and flow conditions exist in this system necessitating the use of different flow models for different geometries and flow regimes. In total, we consider four different model types. First, a system of 1D nonlinear hyperbolic partial differential equations (PDEs) is considered to simulate blood flow in larger arteries with highly elastic vessel walls. Second, we assign 1D linearized hyperbolic PDEs to model the smaller arteries with stiffer vessel walls. The third model type consists of ODE systems (0D models). It is used to model the arterioles and peripheral circulation. Finally, homogenized 3D porous media models are considered to simulate flow and transport in capillaries and tissue within the breast volume. Sink terms are used to account for the influence of the venous and lymphatic systems. Combining the four model types, we obtain two different 1D–0D–3D coupled models for simulating blood flow and transport processes: The first model results in a fully coupled 1D–0D–3D model covering the complete path from the aorta to the breast combining a generic arterial network with a patient specific breast network and geometry. The second model is a reduced one based on the separation of the generic and patient specific parts. The information from a calibrated fully coupled model is used as inflow condition for the patient specific sub-model allowing a significant computational cost reduction. Several numerical experiments are conducted to calibrate the generic model parameters and to demonstrate realistic flow simulations compared to existing data on blood flow in the human breast and vascular system. Moreover, we use two different breast vasculature and tissue data sets to illustrate the robustness of our reduced sub-model approach.

This is an open access article under the terms of the [Creative Commons Attribution](https://creativecommons.org/licenses/by/4.0/) License, which permits use, distribution and reproduction in any medium, provided the original work is properly cited.

© 2022 The Authors. *International Journal for Numerical Methods in Biomedical Engineering* published by John Wiley & Sons Ltd.

**KEYWORDS**

discontinuous Galerkin method, mathematical physiology, mixed-dimensional model, multiscale blood flow models, porous media, transport processes

## 1 | INTRODUCTION

The development of computational models for the simulation of blood flow and transport processes within the human cardiovascular system has become an important field in modern computational medicine. Accurate predictions of flow and transport processes can provide non-invasive options to study and design effective medical procedures for treating several kinds of diseases.<sup>1,2</sup> Invasive medical procedures such as biopsy not only cause damage to healthy tissue but also may yield useful data only at one point in time. *In silico* modeling, on the other hand, is a valuable tool for studying the individual patient's pathophysiology throughout, systematically evaluating and forecasting the outcomes of candidate treatments, and, most importantly, personalizing healthcare. In addition, numerical simulation techniques are used for testing hypotheses; for example, see References [3–8].

To obtain a high fidelity systematic drug delivery surrogate, it is necessary to create a model for blood flow and transport of a solute in the heart chambers, pulmonary circulation, arteries branching out of the heart, as well as the arterial vessels in the breast. In addition, flow and transport models for the vasculature have to be coupled with the corresponding models for the breast tissue that is supplied by the vasculature and possibly contains tumor. Because flow characteristics vary depending on the geometry and mechanical properties of various vascular components, developing a computer model of such complex processes is a challenging undertaking. We describe and implement such flow and transport models in this paper.

Due to the complexity of the vascular tree, it is not feasible to model cardiovascular systems using conventional flow models. The diameters of the larger systemic arteries are centimeters, while capillary diameters are micrometers. Further, large systemic arteries experience turbulent flow while capillary flow has low Reynolds numbers and velocities. To capture the wide variations in both time and length scales in the cardiovascular systems, we employ when feasible simplified flow models of different dimensions and complexity.

The various flow behaviors and vessel features appearing in our vasculature are represented by a combination of 1D partial differential equation (PDE) systems, ODEs, and 3D flow models, which form a 1D–0D–3D coupled model. In contemporary literature, ODEs coupled with higher dimensional models are also referred to as “0D models,” since they contain no space variable. A similar type of modeling approach has been applied, for example, to model flow processes in the brain.<sup>9,10</sup> To compute the flow field within the brain, a three-dimensional (3D) flow model of Darcy type is used. Dimensional reduced models based on one-dimensional (1D) PDEs are coupled with the 3D flow model to provide realistic boundary conditions. Mixed-dimensional models have also shown success in the simulation of flow and transport within small microvascular networks and surrounding tissue.<sup>11</sup> Here, the tissue matrix is again considered as a 3D porous medium and the blood vessel network is approximated by a 1D graph. Contrary to the previous approach the 1D blood vessel network is directly embedded into the tissue matrix, which results in a 3D–1D coupled flow model. The respective model equations are coupled by means of their source terms, where the source term of the 3D model exhibits a Dirac measure concentrated on the 1D network. This modeling approach has been used in Wu et al.<sup>12,13</sup> to model flow and transport in a breast network consisting of smaller arteries as well as breast tissue.

In our model, flow and transport processes in the larger arteries branching out of the heart and the smaller arteries containing the breast are governed by 1D PDE systems. For the larger arteries we use a nonlinear hyperbolic equation to model pulsatile blood flow in vessels with elastic walls, see.<sup>14,15</sup> For the smaller arteries in the breast, a linearized version of this flow model is considered which is valid for small deformations of the vessel diameter. Preliminary research on the coupling of various 1D-flow models appears in Drzisga et al.<sup>4</sup> At the interface between the larger and smaller arteries, we have to create new bidirectional coupling conditions. This coupling places a significant constraint on the time step size, which motivates a low-cost one-directional coupled model. Surrogate models that account for the influence of vessels that are not part of the 1D networks are required at the outlets of the 1D networks. We couple the corresponding 1D models with Windkessel models based on ODEs at the outlets of the nonlinear 1D network to incorporate the capacity and flow resistance of the vasculature located beyond the outlets.<sup>16,17</sup> These models are commonly known as lumped-parameter models, see Fernandez et al.<sup>18</sup> At the outlets of the linear network, we attach surrogate

models for the arterioles that connect the breast network outlets to the capillary bed. New lumped parameter models are developed for these vessel trees.

We consider 3D homogenized models such as those presented in References [9, 10, 19–22] to determine the flow field within the capillaries and tissue. This results in a 3D-3D double continuum model of flow within the breast microvasculature and tissue. Both 3D models are based on the theory of porous media. Because the Reynolds numbers in both the capillaries and the tissue are less than one, Darcy's equation is used to calculate the pressures in both regions. We couple both equations by their source terms to model fluid exchange between the vascular system and the interstitial space of the tissue. By including sink terms in the Darcy equation for the capillary continuum, the influence of the venous system draining the breast tissue is accounted for. For tissue permeability, values from Wu et al.<sup>12</sup> are considered, whereas for capillary bed homogenization, existing results from literature<sup>21–25</sup> are adopted.

Finally, the model for arterioles is coupled with the capillary continuum. Unlike previous models,<sup>9,10,19,23</sup> we do not directly couple the 1D PDEs in the terminal vessels with the continuum, but we employ that the lumped parameter model for the arterioles is coupled with both the 1D PDEs in the terminal vessels and the 3D continuum model for the capillaries. This is required because the pulsatile flow in the breast network must be converted into a non-pulsatile flow that is present in capillaries and tissue. To simulate the propagation of a solute, all flow models must be coupled to either a convection diffusion equation modeling solute concentrations. This is done in References [26, 27] for the larger arteries and the breast network. All other models, particularly the 0D or lumped parameter models, must be augmented by a transport process equation.

This paper is organized as follows: The generic and patient-specific blood vessel networks, as well as the modeling assumptions, are introduced in Section 2. Section 3 describes the mathematical sub-models that adhere to these assumptions and their coupling and boundary conditions are given in Section 4. In Section 5, the vascular data from Section 2, the model from Section 3 and the coupling and boundary conditions from Section 4 are combined into a complex 1D–0D–3D coupled model that contains nonlinear components. This model is referred to as a fully coupled model. Further, we also describe a more efficient computational modeling approach that decomposes our data into a generic patient independent part that only needs to be calculated once and a patient specific part that needs to be recalculated for different breast geometries. Section 6 discusses our numerical solution methods, and Section 7 displays simulation results. We compare the fully coupled model to available medical data and the simplified sub-model. Finally, closing remarks are given and an outlook to future work is described in Section 8.

## 2 | MODEL SETTING

In this section, we describe our data sets and formulate our most significant modeling assumptions.

### 2.1 | Description of the data sets

In order to simulate blood flow and transport processes in the larger systemic arteries branching out of the heart, we use the data<sup>28</sup> as a generic patient unspecific geometry. These data describe an arterial network consisting of 33 arteries and containing the aorta, carotid arteries as well as the Circle of Willis. Moreover, the main brachial arteries and the subclavian arteries are part of this network (see Figure 1, upper left). Table 1 in Alastruey et al.<sup>28</sup> contains the average lengths, radii, wall thicknesses and elasticity parameters of the corresponding vessels. In particular, the subclavian arteries are of great interest for the objective of this paper since they contain several branches supplying blood and other constituents to the breast tissue (see Figure 1, upper right). Therefore, the right subclavian artery and brachial artery of the data set are split into two parts which yield the network in the lower left corner of Figure 1 with the additional Vessels 34 and 35 and the additional branches (see Figure 1, lower left). Hereafter, this network (i.e., the network consisting of Vessel 1, ..., 35) is denoted as macrocirculation, and the set containing all its vessel ids is denoted by  $I_{\text{macro}}$ . The vessels with an outlet are contained in  $I_{\text{macro}}^{\text{out}}$ , while the only inlet at the aorta is assigned to  $I_{\text{macro}}^{\text{in}}$ .

As a patient specific geometry, we use the breast network that can be found in Wu et al.,<sup>12,30</sup> see Figure 1 (lower right). First, a 3D volumetric mask of vasculature was segmented from high-resolution Dynamic Contrast-Enhanced Magnetic Resonance Imaging (DCE-MRI).<sup>12</sup> A multiscale Hessian filter<sup>31</sup> was used to subtract the pre-contrast from the post-contrast, high-spatial resolution DCE-MRI, calculating the probability of each voxel containing a vessel, and then

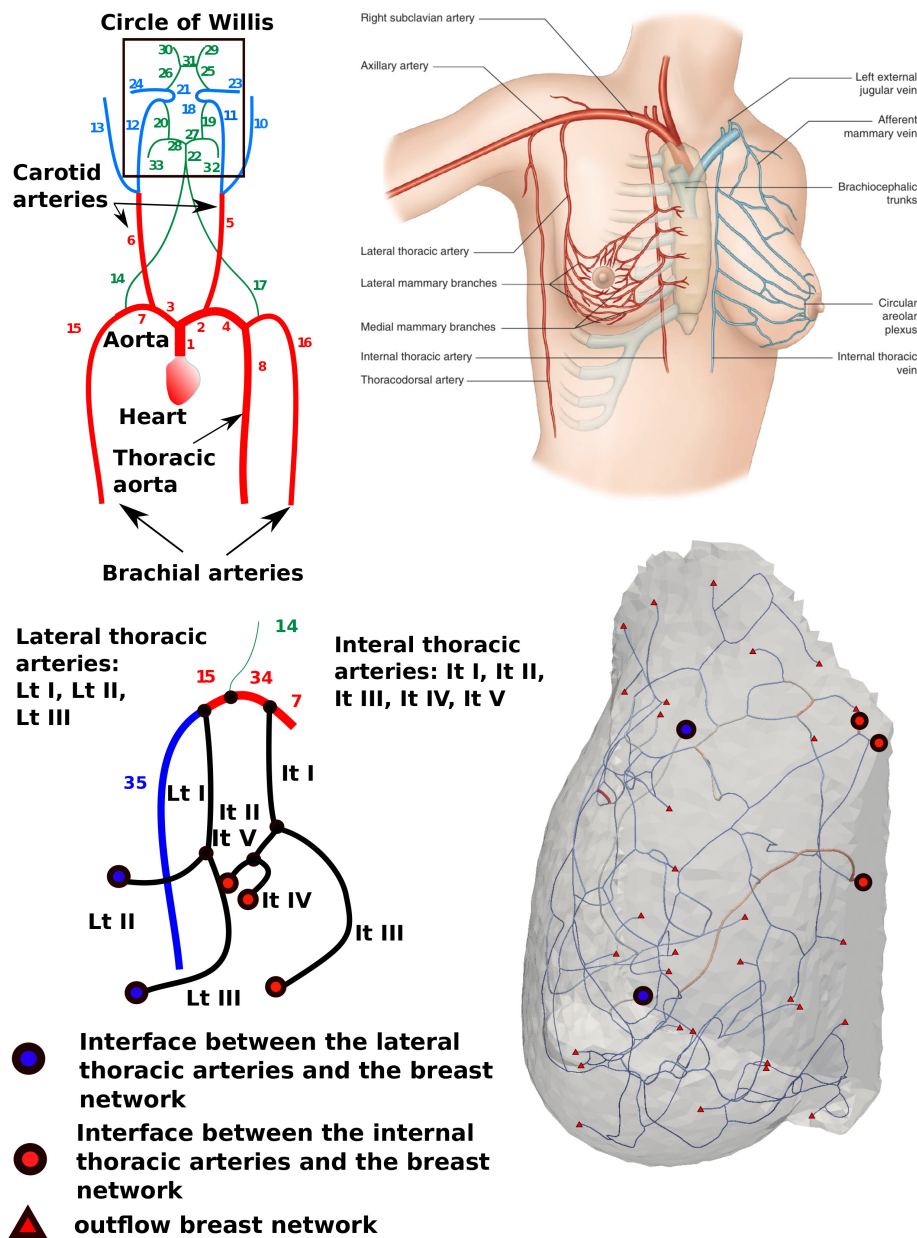


**FIGURE 1** Upper left: idealized network consisting of the main arteries branching out of the heart and the Circle of Willis. Upper right: vasculature supplying the breast tissue. Reproduced from Figure 13.4 from Barral et al.<sup>29</sup> with permission from publisher. Lower left: thoracic arteries branching out of the right subclavian (Vessel 7) and brachial artery (Vessel 15). As a result Vessel 7<sup>28</sup> is split into new vessels having the indices 7 and 34, while Vessel 15<sup>28</sup> is split into 15 and 35. Lower right: a vascular network embedded inside a 3D breast volume. Connections between the thoracic arteries and the 1D breast network are blue for the lateral thoracic arteries and red for the interior thoracic arteries.

a threshold was set to generate a binary mask of vasculature.<sup>12</sup> Second, the segmented vascular mask was skeletonized to its centerline, with the branching points, terminal ends, and vessels in the vascular network identified and the vessel orientation calculated for each vessel. After that, a gap filling process was used to transform the vascular network into a single connected graph.<sup>30</sup> Finally, a moving average of one imaging voxel size (i.e., 0.8 mm) was used to smooth out the vessel centerlines.

The breast network is considered as a graph-like structure that is, the data set comprises a list of 3D coordinates of the branching points, inlets and outlets. In the following, we will refer to them as ‘network nodes’. Additionally, it contains information on the connectivity of the network nodes that is, the edges of the graph are defined by it. An average radius is assigned to each edge.

Considering the size of the radii, it turns out that they range from 0.13 to 0.42 mm. Thus, it can be considered as a network of smaller arteries, see Table 1.1. in Formaggia et al.<sup>32</sup> In the following subsections, this network is denoted as the breast network, and its vessel indices are combined in a set  $I_{\text{breast}}$ . We choose the five largest arteries as inlets and collect their indices in  $I_{\text{breast}}^{\text{in}}$  and the remaining terminal vessels in  $I_{\text{breast}}^{\text{out}}$ .

There is still an information gap between the generic macrocirculation and the patient specific breast geometry which we close by introducing an extension network. According to standard medical textbooks, the blood vessels linking the subclavian arteries and the vasculature contained in breast tissue are called thoracic arteries, see Chapter 13 in Barral et al.<sup>29</sup> and Figure 1 (upper right) below. These consist of two main branches which are referred to as the internal and lateral thoracic arteries. Our construction of the thoracic network is depicted on the right of Figure 1 together with its connections to the macrocirculation and breast networks. We assign the indices of the vessels Lt I and It I to  $I_{\text{tho},1}$ , Lt II and It II to  $I_{\text{tho},2}$  and the remaining vessels to  $I_{\text{tho},3}$  such that  $I_{\text{tho}} = I_{\text{tho},1} \cup I_{\text{tho},2} \cup I_{\text{tho},3}$  contains all indices of the extension or the thoracic vessels.

## 2.2 | Model assumptions

In order to model flow and transport processes from the heart down to the breast tissue, it is necessary to take into account many different vessel types. Considering Figure 2, the systemic vessel tree consists of the aorta, elastic arteries, muscular arteries, arterioles, capillaries, and veins. The exchange of fluid and substances between the vasculature and tissue occurs at the capillary level.

Before the model equations for the different parts of the vascular tree and the tissue are presented, we discuss the most important modeling assumptions and simplifications, which are essential for the design of the mathematical model. In total, eight assumptions for our modeling concept are introduced:

(A1) *Blood flow in the macrocirculation is pulsatile and turbulent. Elastic deformation behavior of the vessel walls is assumed.* According to Table 1.7 in Formaggia et al.,<sup>32</sup> blood flow in most vessels of the macrocirculation exhibits Reynolds numbers that are larger than 1000. Therefore, we assume that turbulent flow is present in this sub-network. Furthermore, flow in these vessels is pulsating (see Figure 2). Since the vessel walls of the larger arteries are highly deformable, a fluid structure interaction (FSI) model has to be considered which couples the flow in the lumen of the vessel with the deformation of the vessel wall.

(A2) *Blood flow in the breast network and extension is laminar and the deformations of the vessel walls are small.* Considering the range of diameters occurring in the breast network, it can be concluded that the breast network consists mainly of small arteries. The Reynolds numbers occurring in these vessels are significantly lower (see Table 1.7<sup>32</sup>) compared to the ones in large arteries. Thus, we can expect laminar flow in these vessels. Moreover, the deformation of the vessel walls is much smaller than that of the larger vessels.

(A3) *Tissue is modeled as a porous medium.* Considering the composition of a tissue block, it can be observed that it is mainly composed of cells, fibers, and interstitial space filled with a fluid similar to blood plasma. The interstitial space exhibits several pores that are connected by pore throats. Therefore, it is reasonable to consider tissue as a porous medium which can be described by REV-based flow models<sup>8,34,35</sup> constructed from Darcy's law.

(A4) *Inertial effects concerning flows in the capillary bed and tissue are not considered.* According to Table 1.7,<sup>32</sup> blood velocity is about 0.1 (mm/s) in the arterioles and venules and about 0.01 (mm/s) in the capillary bed in a human system. Therefore, it is reasonable to assume that the Reynolds numbers are significantly lower than 1.0.

(A5) *Drainage systems are modeled as sink terms.* In (A1) and (A2), we have considered the supply systems for the breast tissue. To remove the fluid mass flowing into the breast tissue, drainage systems are required. Within the systemic circulation, the veins and lymphatic system act as drainage systems. As in the case of capillaries and arterioles, there are no data available describing both the venous and lymphatic system. Due to that, we model these drainage systems by means of sink terms within Darcy's equation for both the capillary bed and tissue. Therefore, the sink term representing the veins is assigned to the capillary system, while the source term for the lymphatic system is added to the tissue model.

(A6) Gravity effects are neglected.

(A7) *Blood is an incompressible fluid.* In general, the density of blood is non-constant, since in microvascular networks the red blood cells are not distributed in a homogeneous way.<sup>36–38</sup> However, in many publications,<sup>8,21,39–41</sup> that are concerned with the modeling of blood flow in microvascular networks, compressibility is neglected with only minor effects on the flow.

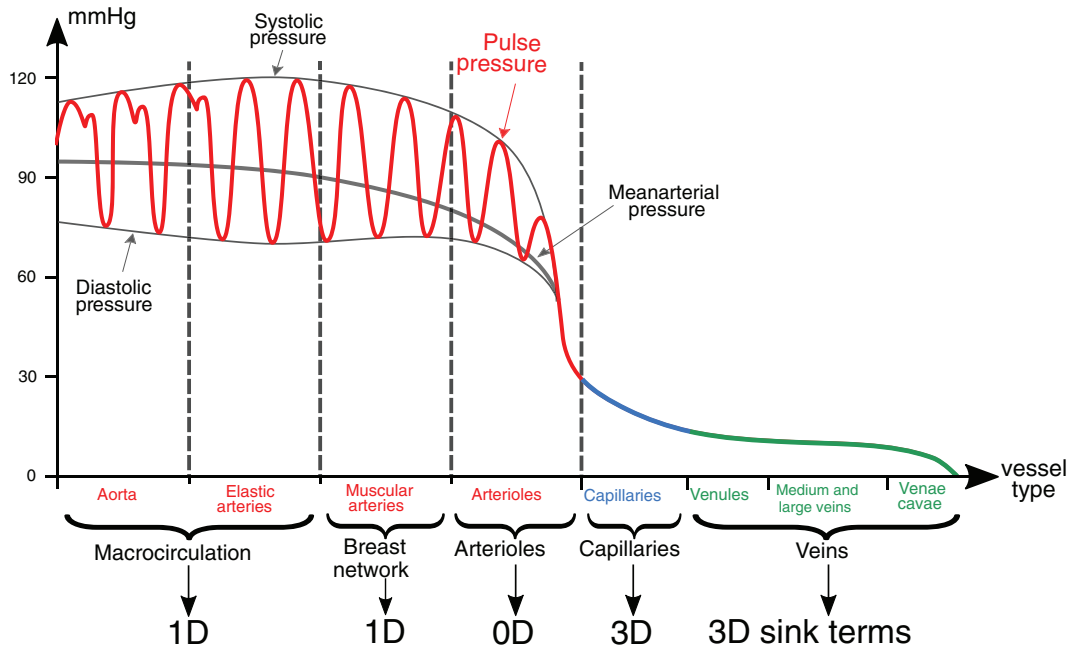


**FIGURE 2** Typical pressure curves within various vessel types in the systemic circulation. In our setting, the aorta and the elastic arteries are partially contained in the macrocirculation, while the breast network is composed of muscular arteries. Flow and transport through both networks are governed by means of 1D models. The remainder of the arterial tree is modeled by lumped parameter models (0D models), homogenized 3D models, and 3D sink terms, resulting in a 1D-0D-3D coupled model. The plot of the pulse pressure is based on Figure 20.10 in Reference [33] (CC BY 4.0).

(A8) *The non-Newtonian flow behavior is accounted for by an algebraic relationship.* Red blood cells govern the viscosity of blood  $\mu_{bl}$  (Pa s) significantly, since the red blood cells have to deform when they move through capillaries. We use the relation<sup>42</sup> which depends on the vessel radius and holds for human blood.

Based on the assumptions (A1)–(A8), we design in the following sections a class of models for flow and transport in breast tissue and its vasculature.

### 3 | MULTISCALE MODEL COMPONENTS

In this section, the model equations for blood flow and transport are introduced, which are based on the assumptions (A1)–(A8) and assigned to different parts of the vasculature.

#### 3.1 | The 1D model

We use reduced 1D models for the parts of the vasculature for which we have topological information describing the connectivity between vessels with known diameters and lengths. Recalling the description of the data sets in Section 2, this is the case for the macrocirculation  $I_{\text{macro}}$ , the thoracic arteries  $I_{\text{tho}}$  and the breast network  $I_{\text{breast}}$ . The single vessels  $\Lambda_i \equiv [0, l_i]$  of length  $l_i$  are considered as one-dimensional manifolds, which are glued together at their boundaries, forming a graph structure. For a time-dependent scalar field  $F$  on the vasculature we denote its restriction to  $\Lambda_i$  by  $F_i$  and its evaluation at time  $t \geq 0$  at  $z \in \Lambda_i$  with  $F_i(z, t)$ .

##### 3.1.1 | The nonlinear model

For the larger arteries contained in  $I_{\text{macro}}$  and  $I_{\text{tho},1}$ , we have to consider assumptions (A1), (A7) and (A8). In order to model blood flow within these vessels, we use a nonlinear hyperbolic PDE model (Equations C2 and C3).<sup>26,43,44</sup> It

describes time-dependent scalar fields for the flow  $Q_i$  ( $\text{cm}^3 \text{s}^{-1}$ ) and vessel area  $A_i$  ( $\text{cm}^2$ ) on each 1D-vessel  $\Lambda_i$ ,  $i \in I_{\text{non}}$ , where  $I_{\text{non}}$  contains the vessel indices on which we impose this model. The resulting velocity fields  $Q_i/A_i$  are then coupled to a 1D transport equation for the line concentration field  $\Gamma_i$  ( $\text{mmol cm}^{-1}$ ) (see Equation C4).

For vessel  $i \in I_{\text{non}}$ , we denote the backward and forward propagating characteristics of the flow problem by  $W_{1,i}$  and  $W_{2,i}$ , while  $W_{3,i}$  is the single, scalar characteristic for the transport problem. These characteristics enable us later to infer coupling conditions. The couplings of the nonlinear model at branching points follows the procedure described in Masri et al.<sup>27</sup>

### 3.1.2 | The linearized model

For smaller vessels further down the vascular tree that is, the vessels contained in  $I_{\text{tho},2}$ ,  $I_{\text{tho},3}$  and  $I_{\text{breast}}$ , the deformations are less significant. Thus, a simplified linearized model can be applied, based on assumptions (A2), (A7) and (A8). We collect the vessel indices for this model in  $I_{\text{lin}}$ . It describes the pressure  $p_i$  (Ba) and flow  $q_i$  ( $\text{cm}^3 \text{s}^{-1}$ ) fields for each vessel  $i \in I_{\text{lin}}$ . The model itself is given by a 1D hyperbolic PDE system (Equations C12 and C13). A derivation is given in Section 6.2.1 in Reference [1]. The resulting velocities  $q_i/A_i$  are coupled to the transport of the concentration  $\Gamma_i$  as in the nonlinear case (see Equation C14). We denote the characteristics for the flow by  $w_{1,i}$ ,  $w_{2,i}$  and for the decoupled transport by  $w_{3,i}$ . Thereby  $w_{1,i}$  is the backward traveling wave, while  $w_{2,i}$  is the forward traveling wave. The coupling of linear models at branching points using characteristics is discussed in Chapter 7 in Reference [1].

## 3.2 | The 3D model

In this subsection, we consider the lowest level within the vascular tree that is, the capillary bed and the tissue matrix. Both systems have to be combined since the capillaries exhibit gaps in their thin vessels such that an exchange between the vascular system and the cells can take place. In order to avoid a discrete resolution of the capillary network, homogenized Darcy-type models have been investigated in the literature.<sup>9,19,22,24,45–47</sup> Following this approach and modeling the lymphatic and venous systems by means of source terms (see Assumption (A5)), one obtains for the capillary bed (3D porous medium, flow problem)

$$\begin{cases} -\nabla \cdot \left( \varrho_{\text{bl}} \frac{\mathbf{K}_{\text{cap}}}{\mu_{\text{c}}} \nabla p_{\text{cap}} \right) = q_{\text{cv}} + q_{\text{ct}} + q_{\text{ca}}, & \text{in } \Omega, \\ \varrho_{\text{c}} \frac{\mathbf{K}_{\text{cap}}}{\mu_{\text{c}}} \nabla p_{\text{cap}} \cdot \mathbf{n} = 0, & \text{on } \partial\Omega, \end{cases} \quad (1)$$

and for the tissue (3D porous medium, flow problem)

$$\begin{cases} -\nabla \cdot \left( \varrho_{\text{int}} \frac{\mathbf{K}_{\text{t}}}{\mu_{\text{int}}} \nabla p_{\text{t}} \right) = -q_{\text{ct}} + q_{\text{tl}}, & \text{in } \Omega, \\ \varrho_{\text{int}} \frac{\mathbf{K}_{\text{t}}}{\mu_{\text{int}}} \nabla p_{\text{t}} \cdot \mathbf{n} = 0, & \text{on } \partial\Omega. \end{cases} \quad (2)$$

Here,  $\Omega \subset \mathbb{R}^3$  denotes the tissue volume, and  $p_{\text{cap}}$  (Ba) and  $p_{\text{t}}$  (Ba) represent the pressures in capillary bed and tissue, respectively. Moreover,  $\varrho_{\text{bl}}$  ( $\text{g/cm}^3$ ) is the density of blood. Following Józsa et al.,<sup>9</sup> the diameter of a capillary is between 5.0 and 10.0  $\mu\text{m}$ . Thus, we can use  $\mu_{\text{bl}}$  from (A8) with an averaged capillary radius  $\bar{r}_{\text{c}} = 3.75 \mu\text{m}$  to define the viscosity  $\mu_{\text{c}} = \mu_{\text{bl}}(\bar{r}_{\text{c}})$ . The permeability tensors  $\mathbf{K}_{\text{cap}}$  ( $\text{cm}^2$ ) and  $\mathbf{K}_{\text{t}}$  ( $\text{cm}^2$ ) have the following shape:  $\mathbf{K}_{\text{cap}} = k_{\text{cap}} \times \mathbf{I}_3$  and  $\mathbf{K}_{\text{t}} = k_{\text{t}} \times \mathbf{I}_3$ , where  $\mathbf{I}_3 \in \mathbb{R}^{3 \times 3}$  is the identity matrix. In contemporary medical literature,<sup>39</sup> a constant value for  $k_{\text{t}}$  is chosen. Following Reference [9], the permeability of the capillary bed can be estimated as follows:

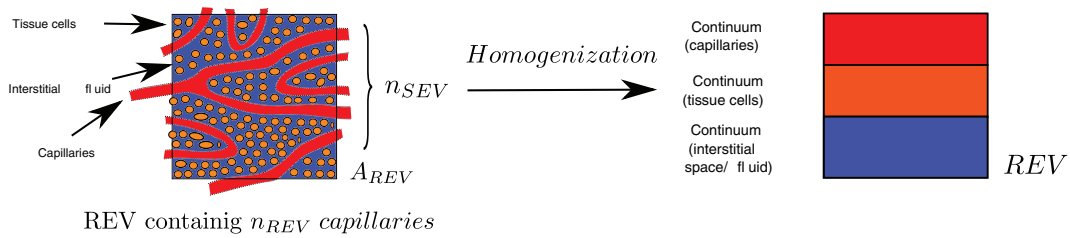


FIGURE 3 Illustration of the capillaries, tissue cells and interstitial fluid, which undergo a homogenization procedure.

$$k_{\text{cap}} = \frac{n_{\text{SEV}} \times \bar{r}_c^4 \times \pi}{8 \times A_{\text{REV}}}.$$

Here,  $n_{\text{SEV}}$  is the number of capillaries passing a facet of a cubed REV, see Figure 3, having the area  $A_{\text{REV}}$ . In References [22, 24], the edge length of a cubed REV is about 1.0 mm. Thus,  $A_{\text{REV}} \approx 1.0 \text{ mm}^2$ .

On the right hand side of (1), three different source terms appear. The first one,  $q_{\text{cv}}$ , accounts for the drainage of the capillary bed by means of the venous vessel systems. Following Chapter 6 in Reference [1], it is given by:

$$q_{\text{cv}} = q_{\text{bl}} \times L_{\text{cv}} \times (p_{\text{v}} - p_{\text{cap}}),$$

where  $p_{\text{v}}$  is an averaged venous pressure.  $L_{\text{cv}}$  (1/Ba s) represents a conductivity parameter for the blood transfer from the capillary system into the venous system. In a next step, we examine the source term  $q_{\text{ct}}$  which includes the flow of blood plasma from the capillaries into the interstitial space of the tissue matrix. To determine this source term, a simplified version of Starling's filtration law is considered. Neglecting the oncotic pressures, it reads as follows<sup>47</sup>:

$$q_{\text{ct}} = q_{\text{int}} \times L_{\text{ct}} \times S_{\text{ct}} \times \left[ (p_{\text{t}} - p_{\text{cap}}) \right].$$

The hydraulic conductivity of the vessel wall is given by the parameter  $L_{\text{ct}}$  (cm s/Ba). Another crucial parameter governing the fluid exchange between vascular system and interstitial space is the surface area per REV:  $S_{\text{ct}}$  (cm<sup>2</sup>/cm<sup>3</sup>). This parameter can be estimated similar to  $k_{\text{cap}}$ :

$$S_{\text{ct}} = n_{\text{REV}} \times 2 \times \bar{r}_c \pi \times \bar{l}_c / V_{\text{REV}} = n_{\text{REV}} \times S_{\text{cap}} / V_{\text{REV}}.$$

Here,  $n_{\text{REV}}$  denotes the average number of capillaries per REV and  $\bar{l}_c$  is the average length of a capillary that is, the average surface area of a capillary is given by:

$$S_{\text{cap}} = 2\pi \times \bar{r}_c \times \bar{l}_c.$$

Moreover,  $V_{\text{REV}}$  denotes the volume of an REV. The last term on the right hand side of (1) incorporates the blood transfer from the arterioles into the capillaries and is described in Section 4.4, since it couples the two models used for these vessel types.

Finally, it remains to specify the source term for the drainage of the interstitial space via the lymphatic system. Here, we assume it is given by:

$$q_{\text{tl}} = q_{\text{int}} \times L_{\text{tl}} \times (p_{\text{l}} - p_{\text{t}}),$$

where  $p_{\text{l}} = 1333.22$  (Ba) and  $L_{\text{tl}}$  (1/Ba s) is again a conductivity parameter for the lymphatic drainage process. In order to model the transport processes within the capillary bed and tissue, two volumetric concentration values

$c_{\text{cap}}$  (mmol/cm<sup>3</sup>) and  $c_t$  (mmol/cm<sup>3</sup>) are considered. Following (A4), the evolution of both concentration variables are governed by stationary convection-diffusion equations. In case of the capillary bed, we obtain:

$$\begin{cases} \nabla \cdot (\mathbf{v}_{\text{cap}} c_{\text{cap}} - D_{\text{cap}} \nabla c_{\text{cap}}) = t_{\text{cv}} + t_{\text{ct}} + t_{\text{ca}}, & \text{in } \Omega, \\ (\mathbf{v}_{\text{cap}} c_{\text{cap}} - D_{\text{cap}} \nabla c_{\text{cap}}) \cdot \mathbf{n} = 0, & \text{on } \partial\Omega. \end{cases} \quad (3)$$

For the tissue matrix, the equations read as follows:

$$\begin{cases} \nabla \cdot (\mathbf{v}_t c_t - D_t \nabla c_t) = -t_{\text{ct}} + t_{\text{tl}} + r_t, & \text{in } \Omega, \\ (\mathbf{v}_t c_t - D_t \nabla c_t) \cdot \mathbf{n} = 0, & \text{on } \partial\Omega. \end{cases} \quad (4)$$

The velocity fields  $\mathbf{v}_{\text{cap}}$  (cm/s) and  $\mathbf{v}_t$  (cm/s) are computed by means of Darcy's law:

$$\mathbf{v}_{\text{cap}} = -\frac{\mathbf{K}_{\text{cap}}}{\mu_c} \nabla p_{\text{cap}}, \quad \mathbf{v}_t = -\frac{\mathbf{K}_t}{\mu_{\text{int}}} \nabla p_t,$$

based on the fluid pressure  $p_{\text{cap}}$  and  $p_t$  from (1) and (2). On the other hand, diffusivity of the transported substance in the capillary and interstitial space is governed by  $D_{\text{cap}}$  (cm<sup>2</sup>/s) and  $D_t$  (cm<sup>2</sup>/s), respectively. As in the case of the flow equations, there are in total four different source and sink terms incorporating the transfer of mass between the different compartments of our model. The first sink term  $t_{\text{cv}}$  (mmol/cm<sup>3</sup> s) models the mass flux from the capillary bed into the venous system. Using the flux  $q_{\text{cv}}$  from (1), the mass transferred from the capillary bed into the venous system, reads as follows:

$$t_{\text{cv}} = q_{\text{cv}} \times c_{\text{cap}}.$$

As in case of the flow problem, the  $t_{\text{ca}}$  term describing the mass flux between the arterioles and the capillary system is discussed in Section 4.4. Furthermore, we have for the lymphatic drainage system:

$$t_{\text{tl}} = q_{\text{tl}} \times c_t,$$

and the exchange between capillaries and interstitial space:

$$t_{\text{ct}} = \begin{cases} q_{\text{ct}} \times c_t, & \text{if } q_{\text{ct}} \geq 0, \\ q_{\text{ct}} \times c_{\text{cap}}, & \text{if } q_{\text{ct}} < 0. \end{cases}$$

The only source term that is not related to source and sink terms of the flow problems (1) and (2) is the reaction term  $r_t$ . For simplicity, we use in this work a simple decay term:

$$r_t = -\lambda_t c_t,$$

where  $\lambda_t$  (1/s) is the corresponding decay rate. Depending on the transported substance more sophisticated reaction terms could be taken into account. In case of oxygen, for example, the Michaelis–Menten law<sup>1</sup> could be considered to model metabolism.

### 3.3 | 0D models

After modeling flow and transport within the larger arteries as well as the microcirculation contained in the breast, we consider in this subsection the remaining parts of the systemic blood vessel system that is, the vessels located beyond the outlets of larger arteries and the arterioles attached to the breast network.

### 3.3.1 | The Windkessel model

Considering the network composed of larger arteries (see Figure 1), it becomes obvious that we neglect a huge number of vessels within the lower body, arms, and head. In order to account for the omitted vessels, we use a Windkessel model described by a surrogate RCR circuit.<sup>16,32</sup> The total resistance and conductance originate from a calibration procedure described in Alastruey et al.,<sup>28</sup> while we take as an input resistance the one of the adjacent 1D vessel to avoid reflections. In addition, the pressure of the veins is required to close the Windkessel model. Recalling (A5), the pressure associated with the veins is approximated by an average pressure  $p_v = 5.0$  mmHg. Therefore  $p_v$  is used to incorporate the flow into the veins. We denote the indices of the involved vessels by  $I_{wk} \subset I_{non}$ .

### 3.3.2 | The tree model

Consistent with the flow regimes indicated in Figure 2, one could see that the pressure within the arterioles decreases significantly and pulsatile flow is transformed into a uniform flow. Since no data is available describing the arterioles between the breast network and the capillary bed, we introduce a surrogate model based on a number of plausible physical assumptions.

Attaching a single Windkessel model to the outlets of the breast network is not sufficient to model the damping effect of the arterioles. Recalling the model equations of the Windkessel model (see e.g., Appendix C.3, (C17)), one can see that the two solution variables of the Windkessel model are given by the averaged pressure of the omitted arterial system and the flow rate from the arteries into the veins. Since the omitted arterial system connects the larger arteries in which pulsatile flow is present and the venules in which no pulsatile flow can be observed, flow in the omitted arteries is partially pulsatile. As a consequence the averaged windkessel pressure can exhibit significant amplitudes. This means that emulating the damping of the pressure between arteries with pulsatile flow and the capillary bed requires either different windkessel models with different parameters or a sequence of windkessel models as in (C16) to account for the heterogeneous flow behavior in the omitted vessels.

A further way to model the arterioles can be found in References [10, 19]. In these publications Darcy type equations are used to emulate the influence of the arterioles. However, in this paper, we consider another approach to avoid ambiguity as to how the permeability tensor of the Darcy-type equation has to be chosen such that the pulsatile pressure in the breast network is damped.

To model the damping effect, we enhance a modeling concept described in.<sup>48</sup> The key idea of this modeling concept is to replace the omitted vessels by a structured tree model. In the remainder of this subsection, we outline the details of this tree model as well as some enhancements to be able to simulate the transport of a solute.

All the indices of the vessels to which the “tree model” is attached are contained in  $I_{tree} \subset I_{lin}$  and we assume that they belong to the terminal vessels of the linearized model. To design a surrogate model for the missing arterioles, we assume for simplicity that the vessel tree attached to a terminal Vessel  $\Lambda_i$ ,  $i \in I_{lin}$  has a symmetric structure. This means that, out of each mother vessel, there are two branches of equal length and radii (see Figure 4).

The issue arises at to how the lengths and radii of the different vessels can be chosen and how many branching levels should be considered. For this purpose, we use an approach described in References [49–54]. Let us denote by  $r_k$  the radius of the vessels within branching level  $k$  and  $l_k$  the corresponding length. For  $k = 0$ , we set the radius of the terminal vessel  $\Lambda_i$  to  $R_i$ . According to literature,<sup>51,52</sup> the radius of a mother vessel  $r_m$  and the radii  $r_{b1}$  and  $r_{b2}$  of the branches are related to each other by the following formula:

$$r_m^\gamma = r_{b1}^\gamma + r_{b2}^\gamma,$$

where  $\gamma \in [2.5, 3.5]$  is a parameter that can be tuned. Since we assumed that the vessel tree is symmetric, it follows:

$$r_{b1} = r_{b2} \text{ and } r_{b1} = r_m \times 2^{-\frac{1}{\gamma}}.$$

This implies that the radii of branching level  $k - 1$  and  $k$  have the following relationship:

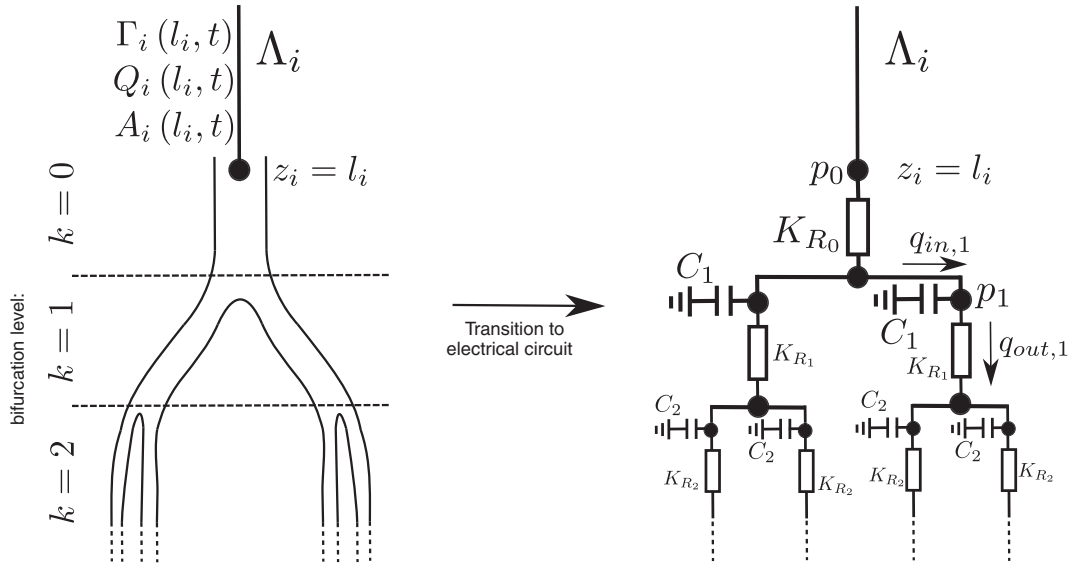


FIGURE 4 Construction of a surrogate model for the arterioles adjacent to a 1D terminal vessel  $\Lambda_i$  using an electrical circuit.

$$r_k = r_{k-1} \times 2^{-\frac{1}{\gamma}}. \quad (5)$$

This recursion also helps us to estimate the number of branching level  $N_{B,i}$ . Using (5) and  $r_0 = R_i$ , we obtain:

$$r_k = R_i \times 2^{-\frac{k}{\gamma}}.$$

In order to estimate  $N_{B,i}$ , we set  $r_k = r_{\text{cap}}$ , where  $r_{\text{cap}}$  is the average radius of a capillary. Therefore, one obtains:

$$N_{B,i} = -\gamma \times \log_2 \left( \frac{r_{\text{cap}}}{R_i} \right).$$

Determining the lengths  $l_k$ , we consider the observation from Schneider et al.<sup>53,54</sup> that there is a fixed ratio  $ra$  between the length and radius of a vessel. This means that the length  $l_k$  is given by:  $l_k = ra \times r_k$ . Here,  $ra$  and  $r_{\text{cap}}$  are given by 28.0 and 5.0  $\mu\text{m}$ , see Table 1.7.<sup>32</sup> Since the surrogate vessel tree is fully symmetric, it is sufficient to calculate the pressures only along a single path and not for the entire tree, yielding a linear complexity in the tree-depth. For a simplified flow model, the tree is converted into an electrical circuit consisting of resistances  $K_{R_k}$  and capacities  $C_k$  on each branching level  $k$  in the tree hierarchy, where pressure and flow-rates correspond to voltage and current, see Chapter 6.1 in D'Angelo.<sup>1</sup> Applying the current-voltage relations for a capacitor on the circuit in Figure 4 yields

$$C_k \frac{dp_k}{dt} = q_{\text{in},k} - q_{\text{out},k},$$

where  $q_{\text{in},k}$  and  $q_{\text{out},k}$  are the flows entering and leaving the  $k$ th vessel and  $p_k$  is the pressure at the capacitor. These are related by Ohm's law to the pressures such that

$$q_{\text{in},k} = \frac{1}{2} \times \frac{p_{k-1} - p_k}{K_{R_{k-1}}}, \quad q_{\text{out},k} = \frac{p_k - p_{k+1}}{K_{R_k}},$$

where the factor 1/2 in  $q_{\text{in},k}$  is due to the fact that the flux through resistance  $K_{R_{k-1}}$  has to split up equally from the parent vessel into the child vessels (see Figure 4). Combining the above equations, we obtain

$$C_k \frac{dp_k}{dt} = \frac{p_{k-1} - p_k}{2K_{R_{k-1}}} - \frac{p_k - p_{k+1}}{K_{R_k}}, \quad k = 1, \dots, N_{B,i}, \quad (6)$$

where the value  $p_{N_{B,i}+1}$  for  $k = N_{B,i}$  is determined by a coupling condition (see Section 4.4). At the other boundary  $k = 1$ , it holds:  $p_0 = p_i(l_i, t)$ . It remains to provide formulas for the computation of  $K_{R_k}$  and  $C_k$ . Therefore, we use the expressions from Chapter 6.1 in Reference [1], which are given by

$$K_{R_k} = \frac{8 \times \mu (2 \times r_k) \times l_k}{\pi r_k^4}, \quad C_k = \frac{3 \times r_k^3 \times \pi \times l_k}{2E_k h_k},$$

where  $E_k$  is the elasticity parameter for the vessels within the  $k$ th branching level,  $h_k$  represents the thickness of the vessel wall, and the viscosity  $\mu$  is again given by (A8). We set  $h_k = 3 \times 10^{-3}$  cm which corresponds to the wall thickness of arterioles listed in Table 1.1.<sup>32</sup> The elasticity parameter was estimated uniformly on all levels as  $E_k = 5.2$  MPa. This value is four times higher than the elasticity parameters of the breast network to simulate the damping effect by the arterioles. All in all, we determine for each time point a vector of pressures  $\mathbf{p} \in \mathbb{R}^{N_{B,i}}$  and flow rates between the different branching levels  $\mathbf{q} \in \mathbb{R}^{N_{B,i}+1}$  given by  $q_k = (p_k - p_{k+1})/K_{R_k}$ .

Having the flow field at hand, a model for transport of a solute in blood can be derived. In a first step, a concentration value  $c_k$  (mmol/cm<sup>3</sup>) and a volume  $V_k$  (cm<sup>3</sup>) is assigned to each branching level. To determine these variables, for each branching level a mass balance equation for the solute and blood volume can be established. In case of the  $k$ th level the equations read as follows:

$$\begin{aligned} \frac{dV_k}{dt} &= \frac{1}{2}q_{k-1} - q_k \quad \text{and} \\ \frac{d}{dt}(V_k(t)c_k(t)) &= N_{k,\text{in}} - N_{k,\text{out}}, \end{aligned} \quad (7)$$

where  $N_{k,\text{in}}$  and  $N_{k,\text{out}}$  are the number of particles in mmol entering and leaving the  $k$ th level per second. Using the flow rates and concentrations of the neighboring vessels we get

$$\frac{d}{dt}(V_k(t)c_k(t)) = \begin{cases} \frac{1}{2}q_{k-1}c_{k-1} - q_k c_k, & \text{if } q_{k-1} \geq 0, q_k \geq 0, \\ \frac{1}{2}q_{k-1}c_{k-1} - q_k c_{k+1}, & \text{if } q_{k-1} \geq 0, q_k < 0, \\ \frac{1}{2}q_{k-1}c_k - q_k c_{k+1}, & \text{if } q_{k-1} < 0, q_k < 0, \\ \frac{1}{2}q_{k-1}c_k - q_k c_k, & \text{if } q_{k-1} < 0, q_k \geq 0. \end{cases} \quad (8)$$

In case of  $k = N_{B,i} + 1$ , the boundary concentration  $c_{N_{B,i}+1}$  is determined by the coupling conditions in Section 4.4. For  $k = 0$ ,  $c_0$  is given by the solution in the 1D terminal vessel  $\Lambda_i$ :  $c_0 = \Gamma_i(l_i, t)/A_i(l_i, t)$ . In total, we have to determine the two vectors  $\mathbf{V} \in \mathbb{R}^{N_{B,i}}$  and  $\mathbf{c} \in \mathbb{R}^{N_{B,i}}$ .

## 4 | COUPLING AND BOUNDARY CONDITIONS

In the previous section, model equations for the different parts of the vascular tree are discussed. It remains to specify the missing boundary and coupling conditions if one of these models is defined on a vessel with an inlet or an outlet.

First, the inflow boundary conditions for the nonlinear model are introduced. For the linearized model, we prescribe a pressure boundary condition at the inlets. The vessel indices at which an inflow boundary condition is applied are contained in the set  $I_{\text{in}}$ . The boundary conditions and the coupling conditions between the different model components remain to be determined. In Section 3.3, the coupling of the Windkessel- and Tree-model with the 1D models in

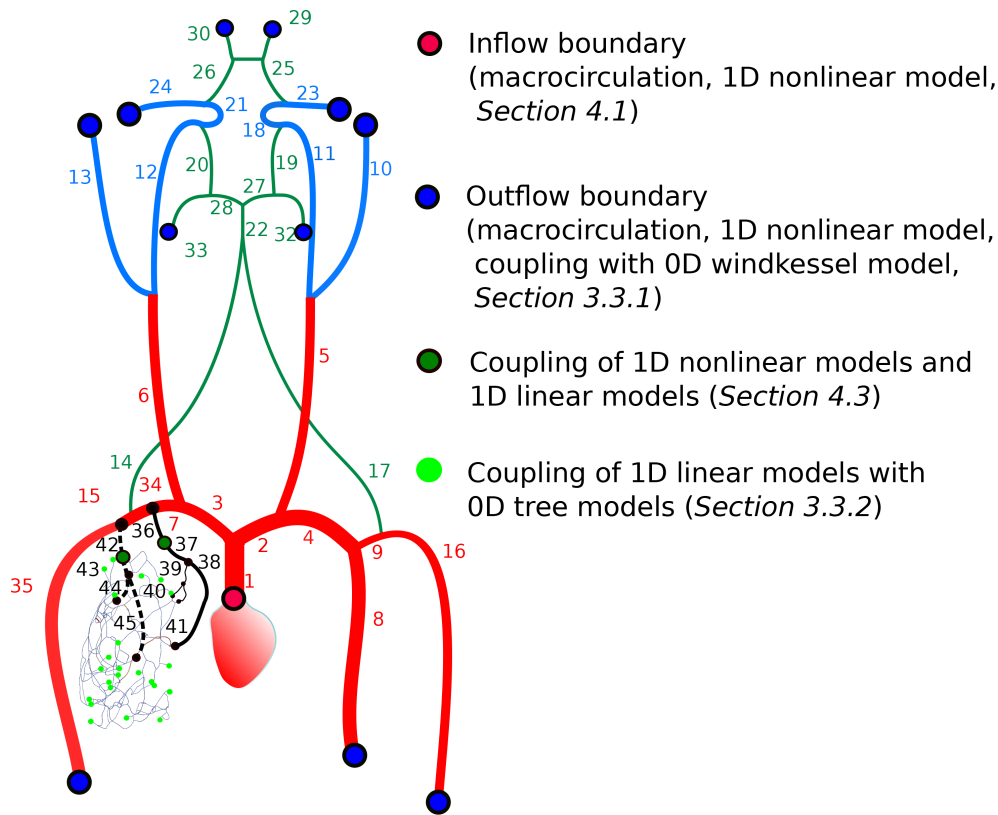


**FIGURE 5** Overview on the coupling concepts for the 1D and 0D models. Red and blue circles indicate inflow and outflow conditions within the macrocirculation network. Dark and light green indicate the coupling of a 1D model to a simplified model.

Coupling of 0D tree models and 3D flow models  
(Section 3.3.2 and Section 4.4)

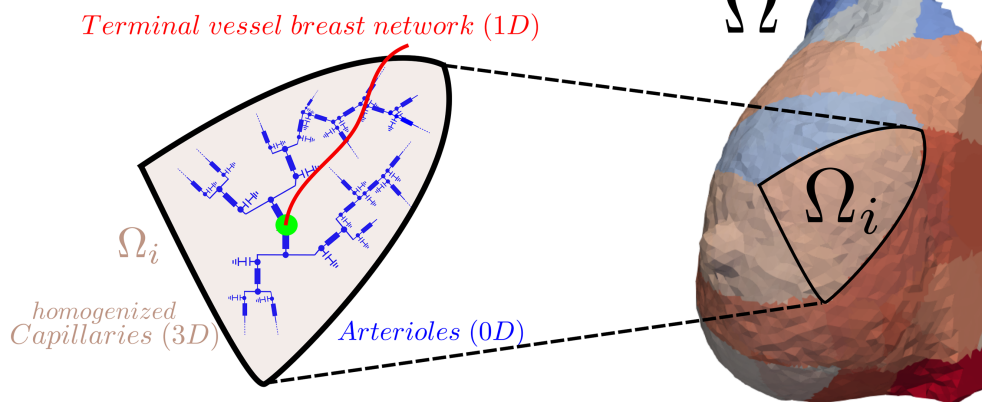


**FIGURE 6** Left: terminal 1D vessel of the breast network supplying the capillary bed contained in a perfusion territory. The arterioles connecting the 1D terminal vessel and the capillaries are modeled by a 0D model (see Section 3.3). Right: perfusion zones of the 3D breast geometry with each zone containing an outlet of the 1D geometry.

the terminal vessels is outlined. The missing coupling conditions between the nonlinear and linearized models are given in Section 4.3. For this, the index sets  $I_{\text{lin}}^{\text{coup}} \subset I_{\text{lin}}$  and  $I_{\text{non}}^{\text{coup}} \subset I_{\text{non}}$  collecting all vessel indices at the interface between the nonlinear and linear model are introduced. Section 4.4 discusses the 0D–3D coupling conditions, of the 0D Tree-models for the arterioles with the 3D porous media models for the capillaries. An overview on the different kinds of coupling can be found in Figure 5 and Figure 6.

## 4.1 | Inflow nonlinear model

Let  $\Lambda_i$  be an inflow vessel in the nonlinear regime that is,  $i \in I_{\text{in}} \cap I_{\text{non}}$ . For convenience, we assume that the parametrization of the vessel  $\Lambda_i$  is oriented in such a way that  $z_i = 0$  is adjacent to the inlet of the aorta. In order to simulate the impact of the heartbeats, we prescribe at  $z_i = 0$  the following profile for the flow rate:

$$Q_{\text{heart}}(t) = Q_{\text{max}} \times \begin{cases} \sin\left(\frac{t \times \pi}{0.3 \times T}\right), & 0 \leq t \leq 0.3 \times T, \\ 0.0, & 0.3 \times T < t \leq T. \end{cases} \quad (9)$$

$Q_{\text{max}}$  ( $\text{cm}^3/\text{s}$ ) is the maximal flow rate and  $T$  (s) is the duration of the heartbeat, which are for our simulations chosen as  $Q = 485 \text{ cm}^3 \text{ s}^{-1}$  and  $T = 1$  s. To determine the flow rate for time points  $T < t$ , we extend  $Q_{\text{heart}}$  periodically. The remaining boundary condition is obtained from the outgoing characteristic variable  $W_{1,i}(0, t)$ . By this, the boundary conditions for  $A_i$  and  $Q_i$  at the inlet can be computed. More details on computing the boundary data at an inflow boundary can be found in literature.<sup>44,55</sup> For the concentration variable, we use a constant concentration value  $c_{\text{in}} = 1 \text{ mmol cm}^{-3}$ , see Chapter 2 in D'Angelo.<sup>1</sup> Thus, we have

$$\Gamma_i(0, t) = c_{\text{in}} \times A_i(0, t), \quad (10)$$

if  $Q_i(0, t) > 0$ . In the other case, an upwinding with respect to the concentration variable has to be performed.

## 4.2 | Inflow linearized model

For each vessel  $\Lambda_i$  with  $i \in I_{\text{in}} \cap I_{\text{lin}}$ , we assume that a time-dependent pressure profile  $\tilde{p}_i(t)$  (mmHg) is given. If we assume again for convenience that  $z_i = 0$  is adjacent to the inflow boundary, then the boundary conditions for flow can be determined from the outgoing characteristic  $w_{1,i}(0, t)$  and the pressure profile  $\tilde{p}_i(t)$ .

## 4.3 | Direct nonlinear to linearized model coupling

Let us consider two vessels  $\Lambda_j$ ,  $j \in I_{\text{non}}^{\text{coup}}$  and  $\Lambda_i$ ,  $i \in I_{\text{lin}}^{\text{coup}}$  where  $\Lambda_i$  and  $\Lambda_j$  are connected and should be coupled. Assuming that  $z_j = l_j$  and  $z_i = 0$ , the outgoing non-linear and linear characteristic variables  $W_{2,i}(l_j, t)$  and  $w_{1,j}(0, t)$  are known, for example, by extrapolation,<sup>56</sup> which yields two coupling conditions. In addition, we enforce the conservation of mass and the continuity of pressure:

$$Q_j(l_j, t) = q_i(0, t), \quad P_j(l_j, t) = p_i(0, t). \quad (11)$$

These equations form a non-linear system of equations for the four boundary values  $Q_j(l_j, t)$ ,  $A_j(l_j, t)$ ,  $p_i(0, t)$  and  $q_i(0, t)$  that has to be solved for time points of interest. By means of the fluid variables, we can determine the concentration variables  $\Gamma_j(l_j, t)$  and  $\Gamma_i(0, t)$ . If the fluid is leaving the respective vessel an upwinding procedure is performed; otherwise, the conservation of solute mass transported through the interface is enforced.

## 4.4 | Coupling between 0D tree and 3D capillaries

The 0D tree model and the 3D capillary model are coupled by suitable source terms  $q_{\text{ca}}$  and  $t_{\text{ca}}$ . In order to define these source terms, we decompose the breast volume into perfusion zones. A similar idea<sup>57</sup> has been considered in context of modeling the myocardial perfusion.

#### 4.4.1 | Perfusion zones

To define so-called perfusion zones, the breast volume  $\Omega$  is decomposed in  $|I_{\text{lin}}^{\text{out}}|$  perfusion volumes which correspond to the number of outlets contained in the linearized model. We denote the perfusion volumes by  $\Omega_i \subset \Omega$  and assume that they form a disjoint decomposition of our 3D-domain that is,  $\Omega = \cup_{i \in I_{\text{lin}}^{\text{out}}} \Omega_i$ . This decomposition is motivated by the fact that each terminal vessel of the breast network supplies blood to a certain tissue volume. Thereby, we assume that the arterioles branching out of a terminal vessel  $i \in I_{\text{lin}}^{\text{out}}$  are distributed in  $\Omega_i$  connecting the breast network and the capillary bed (see Figure 6, left).

Now the challenge arises, how the perfusion areas  $\Omega_i$  can be defined. In context of our modeling approach, we consider the end point  $\mathbf{x}_i \in \Omega$  of a terminal vessel  $i$ . Using this notation,  $\Omega_i$  is defined as follows:

$$\Omega_i = \{ \mathbf{x} \in \Omega \mid \text{dist}(\mathbf{x}, \mathbf{x}_i) < \text{dist}(\mathbf{x}, \mathbf{x}_j), \forall j \neq i, j \in I_{\text{lin}}^{\text{out}} \}.$$

Here  $\text{dist}(\mathbf{x}, \mathbf{y})$  is the Euclidean distance between two points  $\mathbf{x}, \mathbf{y} \in \Omega$ . This definition is motivated by the assumption that a point in the tissue domain is usually supplied by the terminal vessel with minimal distance to this point. The decomposition of  $\Omega$  into the different perfusion areas is shown on the right of Figure 6.

#### 4.4.2 | 0D to 3D coupling

With respect to each perfusion area the source term  $q_{\text{ca}}$  is given by:

$$q_{\text{ca}}|_{\Omega_i} = Q_{\text{bl}} \times L_{\text{ca}} \times (p_{N_{B,i}} - \bar{p}_{\text{cap},i}).$$

$p_{N_{B,i}}$  is the pressure at the tips of the 0D-tree emulating the influence of the arterioles, while  $\bar{p}_{\text{cap},i}$  is the averaged capillary pressure with respect to the perfusion area  $\Omega_i$ :

$$\bar{p}_{\text{cap},i} = \frac{1}{|\Omega_i|} \int_{\Omega_i} p_{\text{cap}}(\mathbf{x}) \, d\mathbf{x}.$$

As in the previous source terms, the pressure difference is weighted by a conductivity parameter  $L_{\text{ca}}$  (1/Ba s). The mass flux from the arterioles into the capillary system is given by:

$$t_{\text{ca}}|_{\Omega_i} = q_{\text{ca}}|_{\Omega_i} \times c_{N_{B,i}},$$

where  $c_{N_{B,i}}$  is the concentration of the last compartment within the 0D tree modeling the arterioles attached to outlet  $i$ .

#### 4.4.3 | 3D to 0D coupling

The back coupling from 3D to 0D is done by setting the boundary pressure  $p_{N_{B,i+1}}$  and boundary concentration  $c_{N_{B,i+1}}$  at the outlets of the 0D-trees to the averaged values  $\bar{p}_{\text{cap},i}$  and  $\bar{c}_{\text{cap},i}$  inside perfusion zone  $\Omega_i$  that is,

$$p_{N_{B,i+1}} := \bar{p}_{\text{cap},i}, \quad c_{N_{B,i+1}} := \bar{c}_{\text{cap},i} = \frac{1}{|\Omega_i|} \int_{\Omega_i} c_{\text{cap}}(\mathbf{x}) \, d\mathbf{x} \quad \text{for all } i \in I_{\text{lin}}^{\text{out}}.$$

## 5 | COUPLED MODELS

After introducing model equations for the different parts of the vascular tree in Section 3 and establishing suitable coupling and boundary conditions in Section 4, we use them to define two different models for flow and transport

processes. The first model is referred to as the fully coupled model (see Section 5.1). It covers the whole flow path from the aorta down to the capillaries and tissue of the breast. After that a sub-model of the fully coupled is defined in Section 5.2 in which only the vascular tree and tissue in the breast are taken into account. In the remainder of this work, it is referred to as the breast model.

## 5.1 | Fully coupled model

We assign the nonlinear model to all the larger arteries as well as to the first two vessels Lt I and It I of our extension. Flow and transport in all the other vessels are governed by the linearized model. We thus have

$$I_{\text{non}} = I_{\text{macro}} \cup I_{\text{tho},1}, \quad I_{\text{lin}} = I_{\text{breast}} \cup I_{\text{tho},2} \cup I_{\text{tho},3}.$$

Conditions (9) are imposed at the inlet of the aorta that is, we set  $I_{\text{in}} = I_{\text{macro}}^{\text{in}}$ . At all outlets of the larger arteries Windkessel models are providing the missing boundary data. Therefore, we have:  $I_{\text{wk}} = I_{\text{macro}}^{\text{out}}$ . The nonlinear and linearized models are coupled with the coupling conditions introduced in Section 4.3. Finally, the linear models in  $I_{\text{breast}}^{\text{out}}$ , the 0D-Tree models and the 3D models for capillaries and tissue are linked together using the coupling conditions from Section 4.3 and 4.4.

## 5.2 | Breast model

To design our breast model, we proceed in two steps: First, we need boundary conditions, which are provided by the nonlinear purely generic model in Section 5.2.1. In the following, this model is called the macrocirculation model. Then, we simulate in a second step (in Section 5.2.2) flow and transport processes in our patient-specific breast network using the linearized PDE model without the generic components. Due to the fact that this model is focused on flow and transport through middle-sized vessels and microcirculation, we refer to it as a meso-microcirculation model.

The first model is based completely on patient-independent data, thus its results can be precalculated and used for all patients. Obviously, not every patient fits the generic data described before, for example, the anterior communicating artery (Vessel 31 in Figure 1) is not always contained in the Circle of Willis. This could be solved by dividing patients into groups sharing similar networks. For each group a generic network could be derived for which the macrocirculation model is precomputed. A new patient would just have to be assigned to one of these groups, before simulations with respect to the individual breast geometry can be taken into consideration. A further advantage would be that the model for the breast is purely linear. Thus, the computational costs are much lower compared to the fully nonlinear model.

### 5.2.1 | Macro-circulation model

To obtain appropriate pressure boundary conditions for the next purely linear model, we only want to simulate the nonlinear model and thus impose

$$I_{\text{non}} = I_{\text{macro}} \cup I_{\text{tho},1}, \quad I_{\text{lin}} = \emptyset.$$

To close the model, we assign Windkessel models to both vessels from the extension network that is,  $I_{\text{wk}} = I_{\text{macro}}^{\text{out}} \cup I_{\text{tho},1}$ . To calibrate the models, we use the algorithm described in Reference [28] with one modification: The compliance and resistance for the right auxiliary artery will distributed between itself, the Lt I and It I vessels. The distribution of the capacities is proportional to the fluid masses leaving these three vessels, while the resistances are distributed in a reciprocal way.

We expect that flows predicted by this nonlinear model will reach a steady state sooner than the fully coupled model. When the pressure and velocity waves become periodic, we can compute the pressures at the outlets  $i \in I_{\text{tho},1}$  for one period and extend them periodically. The tip pressure at vessel  $i \in I_{\text{tho},1}$  defines a boundary condition  $\tilde{p}_j$  for the adjacent vessel  $j \in I_{\text{tho},2}$ .

## 5.2.2 | Meso-microcirculation model

If our data is restricted to the patient specific parts, we obtain the index sets

$$I_{\text{non}} = \emptyset, \quad I_{\text{lin}} = I_{\text{breast}} \cup I_{\text{tho},2} \cup I_{\text{tho},3}.$$

As inflow conditions, we prescribe the pressures at the vessels

$$I_{\text{in}} = I_{\text{tho},2} \subset I_{\text{tho}}$$

as outlined in Section 4.2, with the pressure profiles  $\tilde{p}_i(t), i \in I_{\text{in}}$  defined in the previous section. As in case of the fully coupled model, we combine the 3D and 1D equations using the coupling conditions in Section 4.4.

## 6 | NUMERICAL ALGORITHM

In this section, we first introduce the numerical discretization for the models we presented earlier.

Both 1D-flow models and the transport model are discretized by a second order discontinuous Galerkin discretization in space. The upwinding is determined from the characteristics which can be calculated analytically in our regime.

### 6.1 | 1D-nonlinear flow solver

In time, we use for the nonlinear flow model a 3-step strongly stability preserving method (SSP).<sup>58</sup> The explicit time integrator results in a restriction on the time step sizes due to the Courant–Friedrichs–Lewy (CFL) condition. In case of our application area this is acceptable, since we need small time steps to resolve the pressure and velocity waves. The algorithm is implemented in a matrix-free way using the GMM++<sup>59</sup> and Eigen<sup>60</sup> libraries. For inter process communication, we use the standard MPI primitives.

### 6.2 | 1D-linearized and 0D-tree flow solver

The linearized 1D flow model together with the 0D-Tree model are solved numerically using an implicit Euler scheme in time. Thus, we have no restrictions on the time step size in these regimes. This is convenient in our case, since especially at the beginning of the simulation huge flows from the 3D domain pass the 0D-Tree models and would lead to a severe restriction on the time step size for the 1D model. The implicit-linearized scheme can now act as a buffer between the explicit-nonlinear and the 3D domain making the whole scheme more robust.

For inverting the 1D-linear system, we use the PETSc library,<sup>61</sup> with GMRES as an outer solver and a per processor ILU factorization as a preconditioner. Since all the degrees-of-freedom on a blood vessel get distributed as a whole to one processor the ILU is expected to work well in this case. In addition, since the underlying matrix does not change over time, the factorization has only to be calculated once.

### 6.3 | 1D–1D coupling

The fully coupled model from Section 5.1 needs a direct coupling between the nonlinear and linearized regimes. Thus, both schemes have to work on the same time scale. Their coupling in time is depicted in Figure 7. We first advance the nonlinear scheme with the old characteristic boundary values. The new values from the nonlinear scheme are then fed into the characteristic boundary conditions of the implicit linearized scheme. Using the linearized characteristic as input yields a linear problem, which can be inverted by a standard solver, while using the nonlinear characteristics would result in a nonlinear boundary condition. This requires the usage of a nonlinear solver.

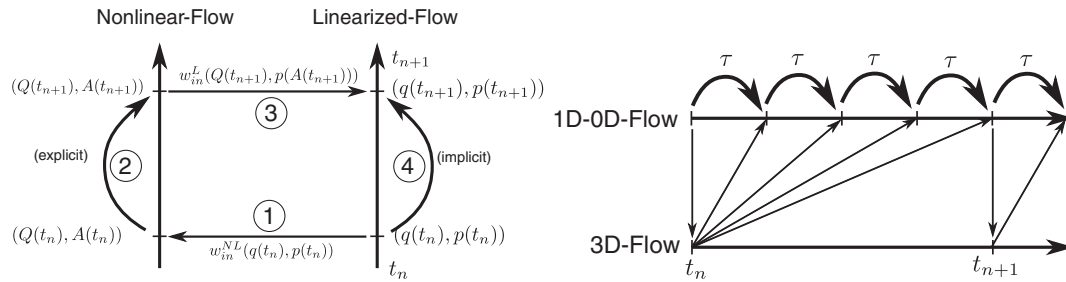


**FIGURE 7** Left: Coupling of the nonlinear-explicit and linearized-implicit 1D schemes in time. Here,  $w_{in}^L$  and  $w_{in}^{NL}$  represent the incoming characteristics of the linearized and nonlinear models. Right: A simple multi-rate time stepping scheme. After several 1D time-steps, the boundary conditions of the 3D Darcy equation are updated and evaluated. The new average 3D pressures at the vessel outlets are used as new boundary conditions for the linearized 1D flow.

Note that with this coupling the explicit nonlinear solver still restricts the time step size of the linearized solver. This is not the case with the model introduced in Section 5.2.2 whose 1D discretization is purely implicit and thus exhibits no time step restriction.

## 6.4 | 0D–3D coupling

For the spatial discretization of the 3D capillary flow problem, we use the space of continuous piecewise-linear polynomials as ansatz functions. The matrices are assembled in FEniCS. To retain the sparsity of the system one additional scalar variable per compartment is introduced which holds the pressure to an average value. The coupling between 0D and 3D is depicted in Figure 7. Due to the small time steps used in terms of the 1D systems, the 3D system is not solved in every time step. Hence, we apply a very basic multi-rate time stepping scheme, which only update the 3D pressures after the time period  $\tau_{3D}$  and then update the 1D boundary condition. This crude coupling works, due to the small changes of the averaged 3D-pressure in time. We solve the 1D systems until the solutions become periodic at a time point  $t_{init,1D}$ . After that, we activate the 0D–3D coupling and simulate until the flow simulation shows a periodic behavior.

## 6.5 | Transport solvers

For a time integrator for the 3D, 1D, and 0D models, we use the implicit Euler method. Since the transport processes in the breast capillaries and tissue are slower compared to the transport process in the vascular tree, we use in case of the 3D models a larger time step size, which aligns with the one for the flow problems. The 3D and 0D transport models are coupled in the same manner as the flow solver. Discontinuous Galerkin methods are used to discretize the 1D model equations in space, while standard linear finite elements are considered for the 3D model equations. The discontinuous Galerkin method has to be combined with a slope limiter technique in order to avoid the formation of spurious oscillations in the vicinity of steep gradients.<sup>62,63</sup>

## 6.6 | Overview of the numerical scheme

Here, we summarize and discuss how the individual components are combined. This is done in Figure 8 for the flow problems and in Figure 9 for the transport. The columns of the table correspond to the different vessel types in our blood flow model. Each of our three flow models is divided into five rows:

In the first three rows, we assign the respective models from Section 3, state their primary variables and their spatial discretization. For the main arteries and parts of the thoracic arteries of the fully coupled model, we assign the nonlinear model from Section 3.1.1 with the vessel area  $A$  and blood flow  $Q$  as primary variables, which are each discretized by second order discontinuous Galerkin elements ( $DG_2$ ). Similarly, we assign the linearized model from

Section 3.1.2, with pressure  $p$  and flow  $q$  to the breast network. For the arterioles we use the 0D-tree model from Section 3.3, which consists of  $N_{B,i}$  scalar pressure values  $p$  at each outlet  $i \in I_{\text{lin}}^{\text{out}}$ , where  $N_{B,i}$  is the depth of the 0D-tree. Finally, we use the 3D-model from Section 3.2 with the capillary pressure  $p_{\text{cap}}$ , the tissue pressure  $p_{\text{tis}}$  and the pressure averages  $\bar{p}_{\text{cap}}$  at each outlet. We use continuous, piecewise linear functions ( $P_1$ ) for the pressure fields and real scalar variables for the averages.

In the fourth row, we specify the applied time integrators to the spatially discretized sub-models. A 3-step SSP-method is assigned to the 1D-nonlinear model (Section 6.1), while the 1D-linearized model and 0D-tree model are

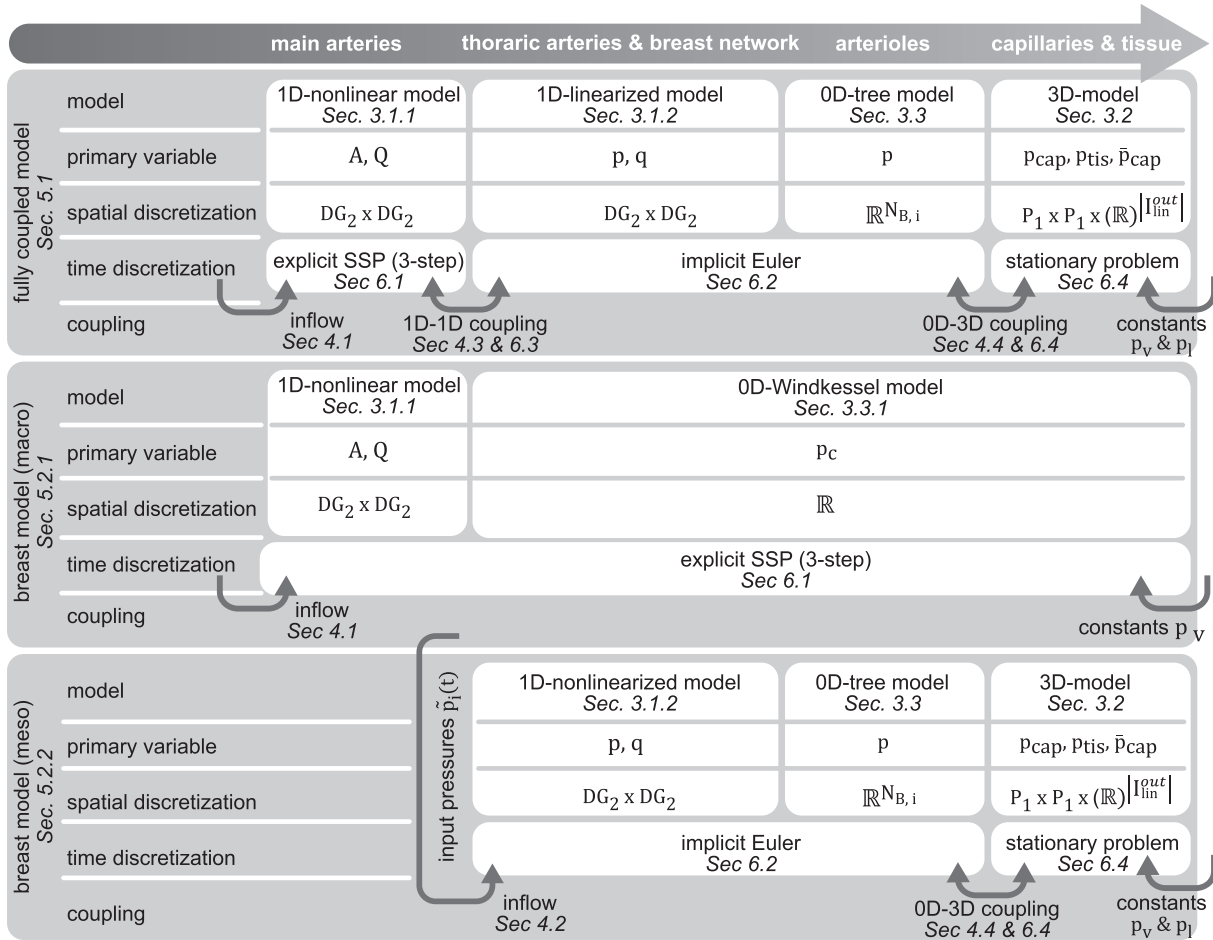


FIGURE 8 From macroscopic flow models to discretized models in time and space.

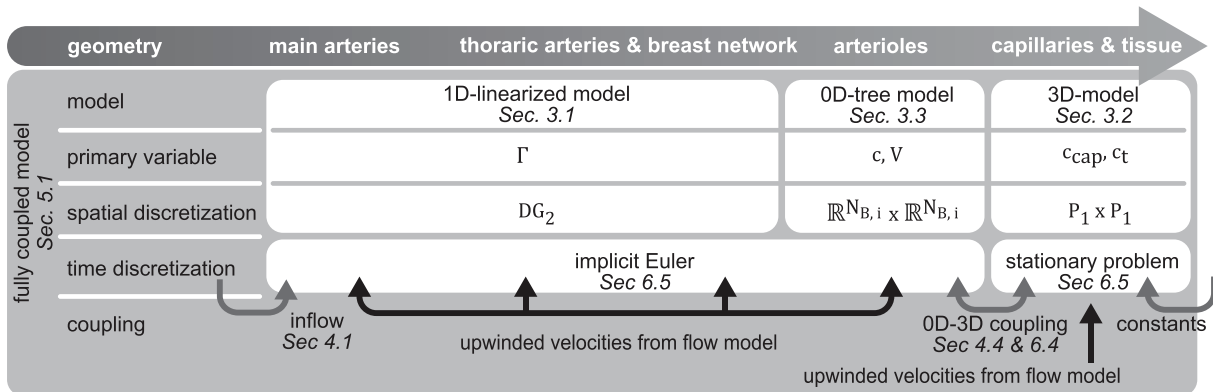
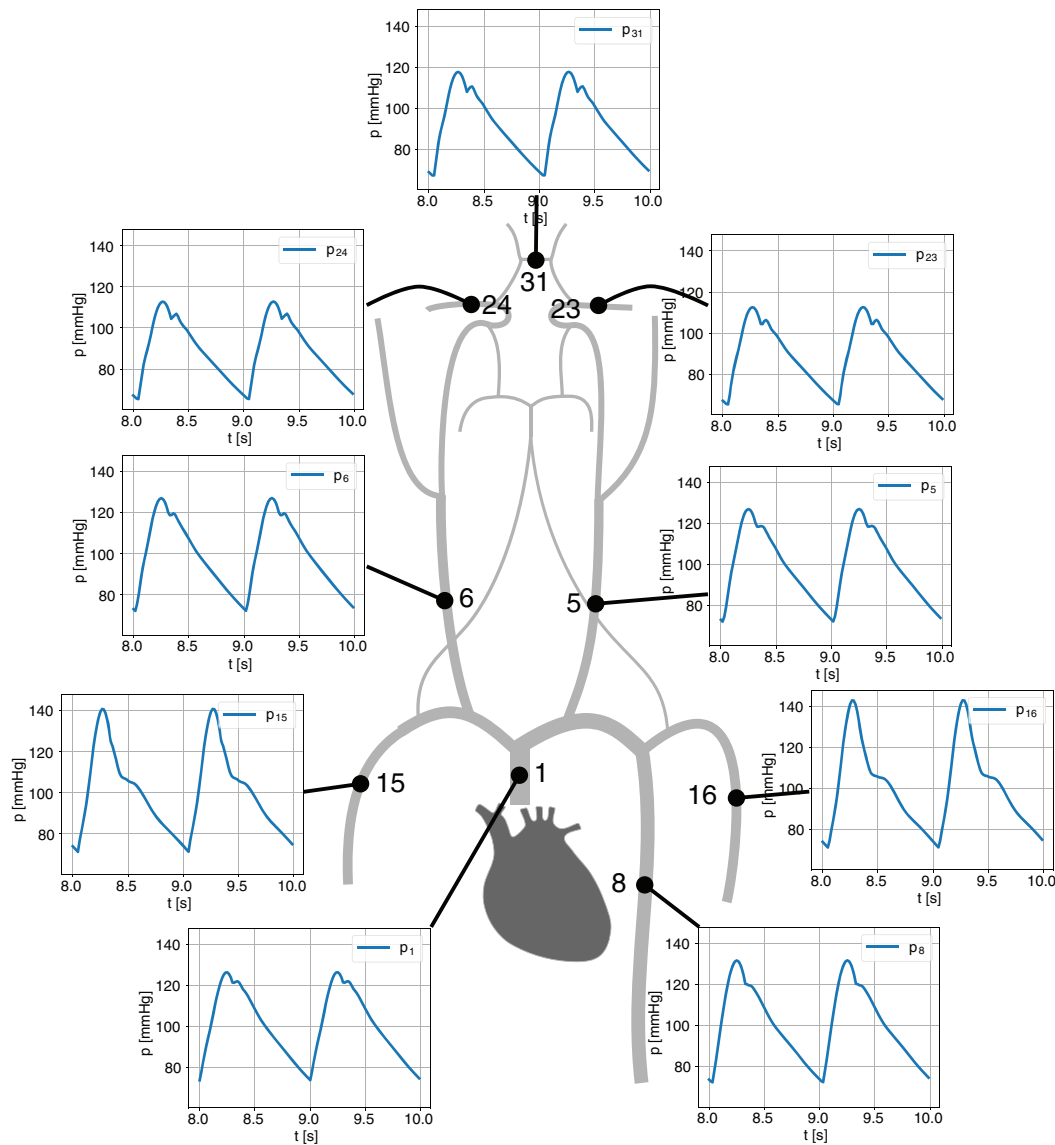


FIGURE 9 From macroscopic transport models to discretized models in time and space.



**FIGURE 10** Pressures (mmHg) and flows ( $\text{cm}^3/\text{s}$ ) at vessel midpoints in the nonlinear regime around the Circle of Willis from 14 to 16 s.

combined and discretized by an implicit Euler scheme (Section 3.1.2). No time integrator is assigned to the time-independent 3D-model.

Finally, in the fifth row, the coupling conditions between the different time integrators are depicted by arrows in which the arrow head denotes the direction of the coupling. Unidirectional couplings from outside are the inflow boundary condition (Section 4.1) and the vein  $p_v$  and lymphatic pressures  $p_l$  which couple to our 3D-model (Section 3.2). Both the 1D-1D coupling between the explicit and implicit schemes (Section 6.3), as well as the 0D-3D coupling between the implicit scheme and the stationary 3D-model (Section 6.4) are bidirectional and hence depicted by arrows in both directions.

For the macro-circulation of the breast model we see that the 1D-linearized model, 0D-tree model, and 3D-model are replaced by the 0D Windkessel models from Section 3.3.1, which model the remaining vasculature by a single averaged capillary pressure  $p_c$ . Only the inflow boundary conditions and the vein pressure  $p_v$  couple into the model.

The meso-circulatory part of the breast model consists of the discretized fully coupled model without the 1D-nonlinear model. Instead, a unidirectional arrow points from the macro-circulation model to the meso-circulation model and indicates, that the time-dependent pressure values  $\tilde{p}_i(t)$  at the tips of the 1D-nonlinear model are used as boundary conditions for the 1D-linearized model.

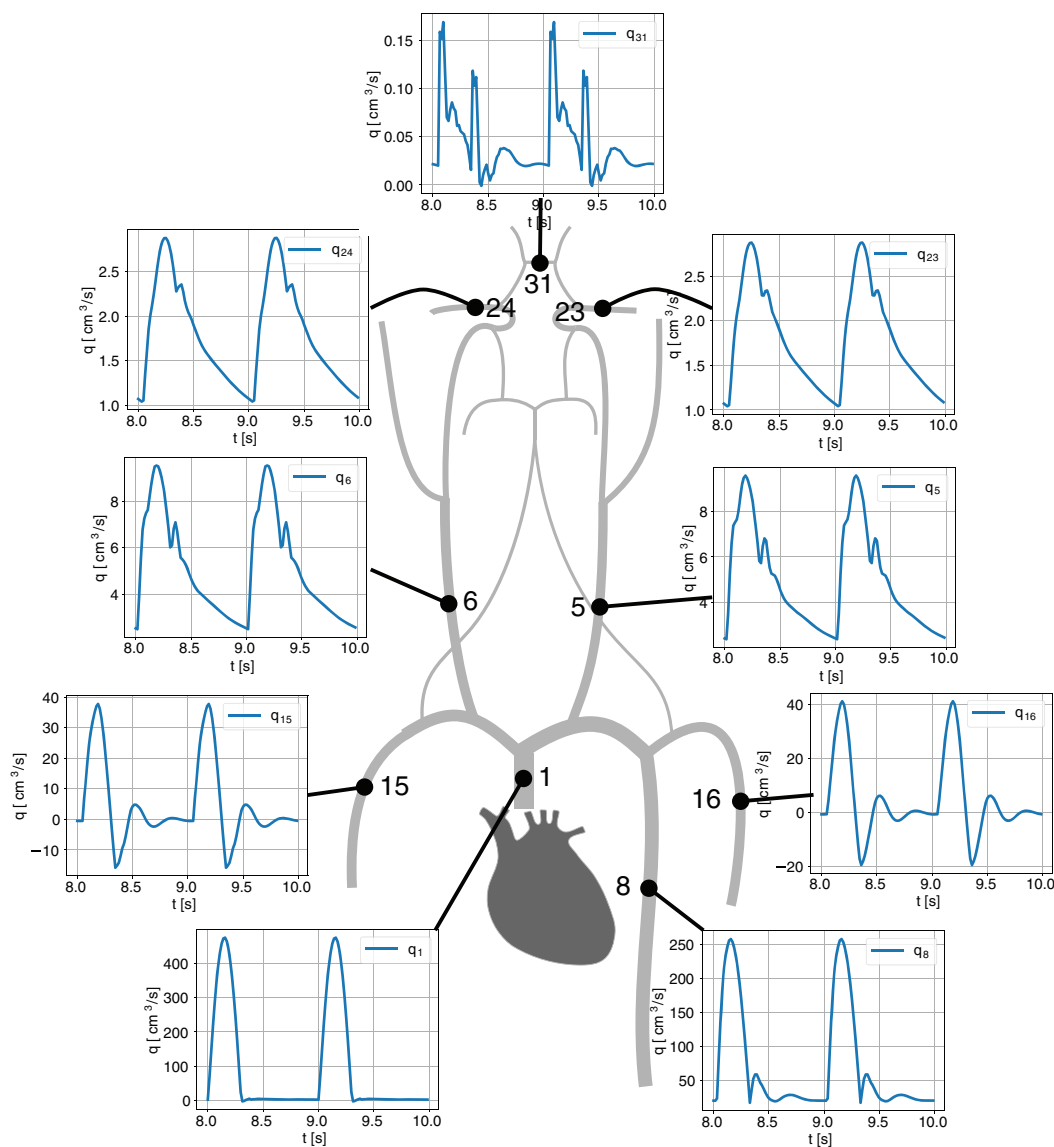


FIGURE 10 (Continued)

In Figure 9, we give a similar overview for the transport model. We assign the 1D-linearized models from Sections 3.1.1 and 3.1.2 to the complete vascular network. Here, the line concentration  $\Gamma$  is the primary variable, and it is discretized by  $DG_2$  elements. The arterioles are modeled with the 0D-models from Section 3.3, which consists of  $N_{B,i}$  concentration  $c$  and volume  $V$  values at each outlet  $i \in I_{\text{lin}}^{\text{out}}$ . For the capillaries and tissue, we use the 3D-model (Section 3.2) with the homogenized concentration fields  $c_{\text{cap}}$  and  $c_t$  in the capillaries and tissue matrix. As a spatial discretization we again rely on  $P_1$  elements.

We discretize in time the combined 1D-linearized and 0D-tree model with the implicit Euler scheme (Section 6.5). No time integrator is needed for the stationary 3D-model.

Again, the inflow values at the heart couple into the system as well as concentrations in the lymphatic  $c_l$  system and the veins  $c_v$ . The latter do not play any role in practice due to the direction of the flows into the lymphatic system and into the veins. Thus they are not part of our discretization. In addition, the upwind velocities from the flow model couple into the transport, which is depicted by black coupling arrows. The only bidirectional coupling between time integrators is between the 0D and 3D models which follows the strategy from Section 6.4.

## 7 | RESULTS AND DISCUSSION

The results obtained using our fully coupled model are first presented and then compared to available biological data by moving through the vessel hierarchy, starting at the inlet of the aorta and ending at the homogenized capillaries. Since the fully coupled model is considered to be our reference model, the results are compared to the simpler breast model, in particular the meso-microcirculation model. This allows us to assess the quality of this sub-model. The source code underlying all numerical experiments, including data for testing, is available at <https://github.com/CancerModeling/Flows1D0D3D/releases/tag/v1.0>.

As model parameters, we use  $\rho_c = 0.997$  and  $\rho_t = 1.060 \text{ g cm}^{-3}$  for the densities of blood in the capillaries and tissue. We estimate  $S_{ct}$  by assuming  $n_{REV} = 460$  which is a lower estimate for the capillary density in muscles,<sup>64</sup>  $\bar{r}_c = 3.375 \times 10^4$  and  $\bar{l}_c = 0.06 \text{ cm}$ . We set  $k_{cap} = 1 \times 10^{-9}$  and  $k_t = 1 \times 10^{-14} \text{ cm}^2$  from Table 1 in Vidotto et al.<sup>22</sup> For the mean vein and lymphatic pressures we assume  $p_v = 10 \text{ mmHg}$  and  $p_l = 1 \text{ mmHg}$ . Applying Ohm's law to the last compartment of the 0D model and averaging yields

$$L_{ca} = \frac{Q_{bl}}{|I_{breast}^{out}|} \sum_{i \in I_{breast}^{out}} \frac{1}{|\Omega_i|} \frac{2^{N_{B,i}}}{K_{R_{N_{B,i}}}}, \quad (12)$$

as an estimate for  $L_{ca}$ . The remaining permeabilities are set to  $L_{cv} = L_{tl} = 10^{-8} \text{ Ba}^{-1} \text{ s}^{-1}$  and  $L_{ct} = 10^{-9} \text{ cm s Ba}^{-1}$ . For the transport we use the oxygen specific values  $D_t = 1.7 \times 10^{-5} \text{ cm}^3 \text{ s}^{-1}$  and  $\lambda_t = 6 \times 10^{-5} \text{ s}^{-1}$  from Reference [1] and set  $D_c = D_t$ .

The numerical parameters for the fully coupled model are set to  $\tau = 2^{-16} \text{ s}$ ,  $t_{init,1D} = 6 \text{ s}$  and  $\tau_{3D} = 2^{-3} \text{ s}$ . The boundary condition for the transport is activated after 6 s.

### 7.1 | Fully coupled model

Results related to the 1D flow models are presented first. In Figure 10, the pressures and flow rates in the nonlinear regime of our model are depicted, which contains the circle of Willis.

This scenario describes a good benchmark test for the nonlinear part of our model. The pressure at the entrance of the aorta is 130/80 mmHg, while the pressures in the arm arteries are a little higher at 140/80 mmHg, both of which are well within a physiologically meaningful regime. While the order of magnitude of pressure values stays constant in the whole nonlinear regime, the same is not true for the flows, which depend strongly on the vessel diameter. Flow rates of up to  $500 \text{ cm}^3 \text{ s}^{-1}$  leave the heart and thus most of the blood flows into the lower torso (77%), the head (13%) or the arms (10%). Only a small fraction of 1.2 per-mille, reaches the breast. The flow through the ‘‘anterior communicating artery’’ at the very top, connecting both parts of the Circle of Willis, is very small. This vessel typically only acts as a backup in case one of the inflows to the brain fails, and our prediction matches medical knowledge. The pressures and flows in Vessels 5 and 6, 23 and 24 as well as in 14 and 16 are nearly the same. This is due to the high spatial symmetry of the underlying vasculature and is to be expected for a valid model.

Figure 11 depicts the flow through the artificial vessels connecting the larger arteries with the measured breast geometry. A periodic behavior is observed and flows have a similar shape. Compared to the flows into the brain, arms, and lower torso, the flows into the breast are small, but always positive and therefore continuously provide blood to the breast. The high frequency components of the flow are quite possibly due to reflections at the vessel boundaries, since the arm arteries have a much larger diameter than the artificial arteries to the breast.

In Figure 12, the pressures and flows of the linearized model for a single flow path starting at an inlet connected to the nonlinear regime and ending at an outlet connected to our lumped parameter models are shown. It is observed that approaching the outlet, the average pressure is slowly damped down. Starting at 123/75 mmHg, it gets damped down to 70/45 mmHg. The flow on the other hand decreases much faster, since it strongly depends on the size of the vessel which visibly decreases. Also, the high frequency components of the flow, which are visible near the coupling points and are still prominent near the inlet, get smoothed in space so that the flow reaching the outlets already appears very smooth.

In Figure 13, pressures inside the vessels of 0D-Tree models are depicted. Every subplot belongs to one lumped vessel in the hierarchy, where the leftmost vessel interacts with the linearized 1D model, while the rightmost vessel is

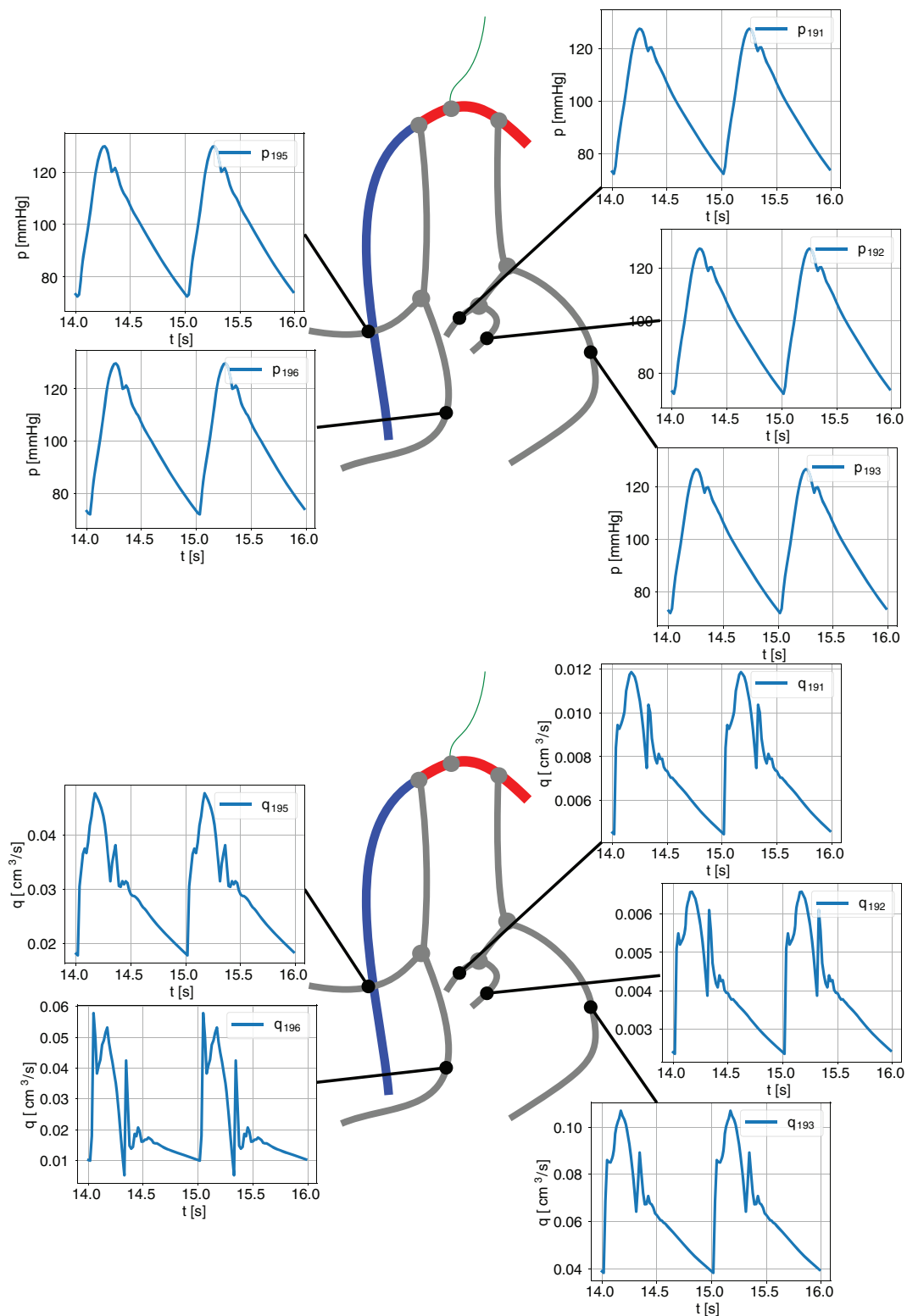


FIGURE 11 Pressure and flow rates within the artificial vessels connecting the large arteries with the breast geometry.

coupled to the 3D homogenized capillary domain. The time interval contains two heart beats from 14 to 16 s. After 14 heart beats, the solution is already periodic in all the compartments of our vascular tree. In addition, a large drop in the pressure amplitude from about 16–0.5 mmHg is observed. The pressures in the last compartment falls into the range of capillary pressures in Figure 2.

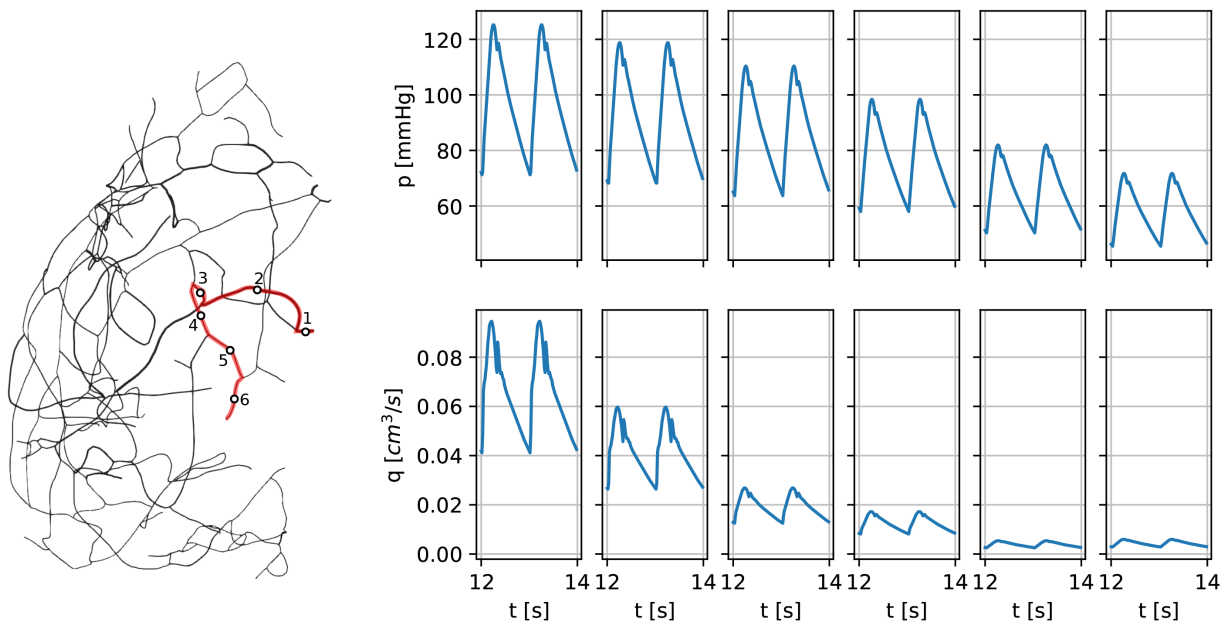


FIGURE 12 Pressures (upper right) and flows (lower right) through one exemplary path in the breast geometry (left).

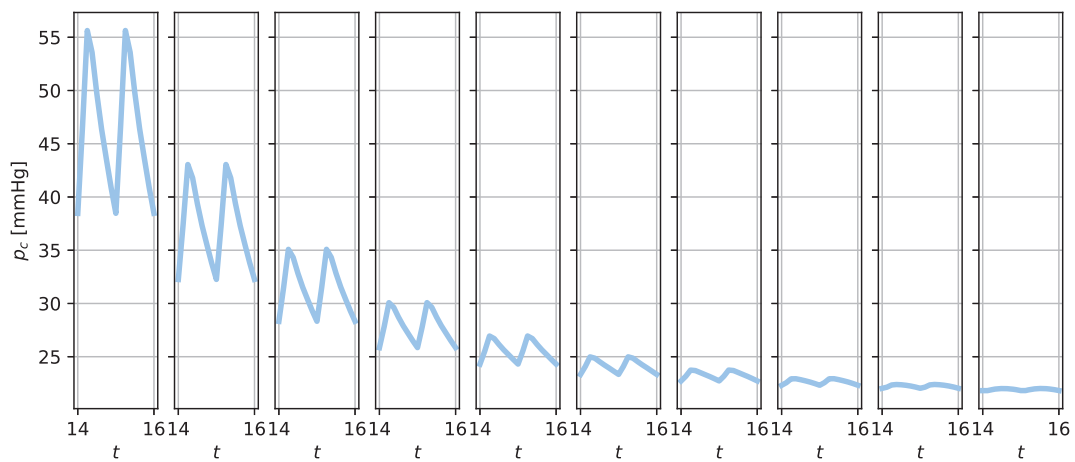
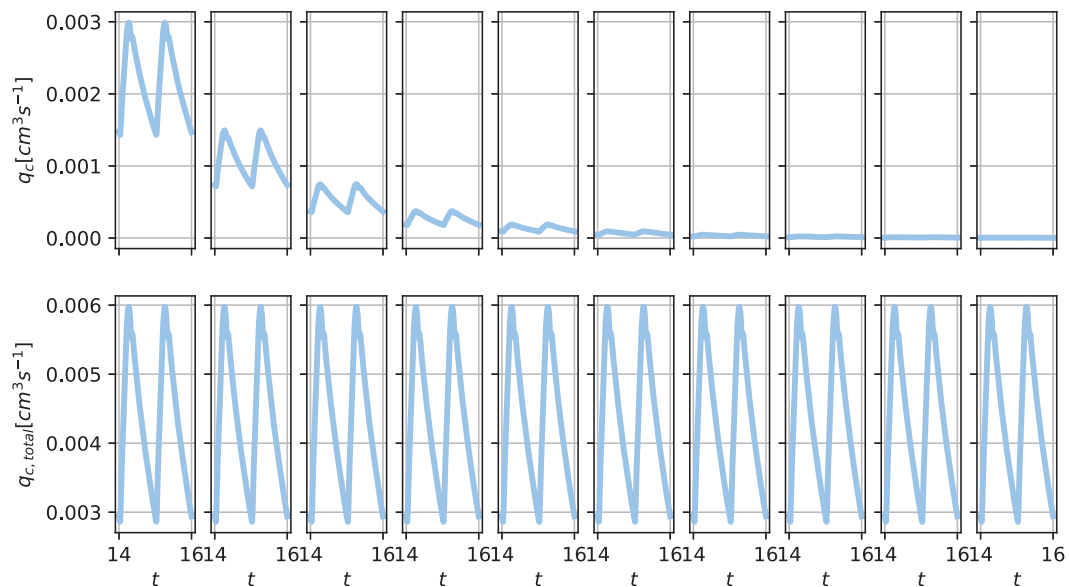


FIGURE 13 Pressure decay within a 0D-tree model. For each compartment the pressure waves for two heart beats are shown.

In Figure 14, additional results on the flow inside the vessels of our 0D tree models are shown. As can be seen in the upper row, for a single vessel the flow decreases by one half from one compartment level to the next due to the bifurcation. Multiplying the flow by the number of vessels on each level replicates the total flow. The bottom row in the figure shows that the total flow is conserved. Integrating the total flow of all 0D models over time yields that  $1.3 \times 10^{-1} \text{ cm}^3$  of blood leave the 0D-networks every heartbeat. The blood volume leaving a single 0D network is between  $1.3 \times 10^{-3}$  and  $8 \times 10^{-3} \text{ cm}^3$ .

In Figure 15, the pressure amplitude on the left, as well as the mean, maximal, and minimal pressure values in our 1D and 0D models are shown. The color gets lighter from the nonlinear, over the linearized to the 0D tree-models. In 1D, the pressures are measured at the center of the vessels, and for the varying radii in the nonlinear regime, we use the one at zero pressure. For large and medium-sized arteries, the pressure amplitude stays in the same range at 55 mmHg, and we have a stable mean pressure just below 100 mmHg. Our model can replicate the effect that the pressure does not attain its maximum at the aorta, but in the brachial arteries, where we reach a pressure amplitude of 72 mmHg. For smaller arterial vessels, we see a pressure drop from 50 to 7 mmHg, which is smeared out over a large range of different pressure values. Here we enter the arterioles, which are modeled by means of lumped parameter models. The pressure amplitude decreases significantly, and the mean pressure values converge for smaller radii until



**FIGURE 14** The graphs show the flow rates in one prototypical vessel of the 0D tree over time. Top: flow rate in one vessel on each bifurcation level. Bottom: total flow in all vessels of the tree belonging to one bifurcation level.

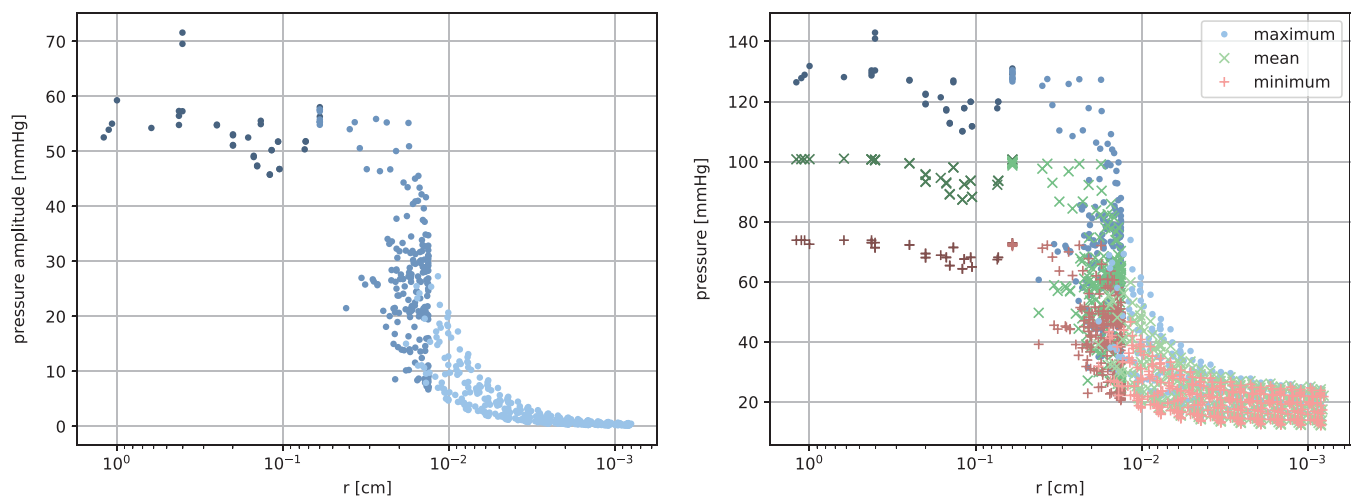


**FIGURE 15** Plot of the vessel radii of the nonlinear, linearized and 0D flow models against the pressures which were averaged from heart beat 14 to heart beat 20. To differentiate between the models, the color value gets lighter from the nonlinear over the linearized to the 0D model. The left plot shows the pressure amplitude in this time interval, while the right shows the maximum, mean and minimum pressures for all radii.

they are in a range between 25 and 12 mmHg. Both plots are in agreement with the expected qualitative results of Figure 2. It can be observed that the input pressure for the arterioles is around 30 mmHg and that the pressure amplitudes decrease significantly.

To test the transport model, a time-independent source of  $1 \text{ mmol cm}^{-1}$  is placed at the aortic entrance. The concentration front propagates through the whole network, mostly during the systolic phase of the cardiac cycle. Figure 16 depicts the transport inside the 0D trees. The upper row depicts the concentration inside the compartments. The concentration front enters the tree around heart beats eight and propagates nearly instantaneously through the whole tree. At heart beat 14 it has reached a fixed value of  $1 \text{ (mmol/cm}^3\text{)}$ . The middle row shows the amount of substance in mmol in each compartment, while the lower row shows the total amount of substance stored in all vessels of our tree at a given hierarchy level. Both quantities decrease from one level to the next level. Thus, only a small amount of mass is stored in the arteriolar trees. Combining these results with the flow rate of approximately  $2.25 \times 10^{-3} \text{ cm}^3 \text{ s}^{-1}$  at the tip of our tree from Figure 14, suggests an average flow rate of  $2.25 \times 10^{-3} \text{ mmol s}^{-1}$  from our trees into the 3D domain.

In Figure 17, we see the concentration in capillaries and tissue of our perfusion domains. When a concentration front arrives at the vessel tips it starts to spread uniformly in its domain. The capillary concentration approaches a constant value of  $1 \text{ mmol cm}^{-3}$ , while the asymptotic mean tissue concentrations vary between 0.6 and  $0.8 \text{ mmol cm}^{-3}$ .

## 7.2 | Breast model

Next, results delivered by the much cheaper uncoupled breast model are compared with the fully coupled model. Figure 18 compares both models in Lt I, It I and Lt II, It II. For the pressure we observe for all four cases an excellent

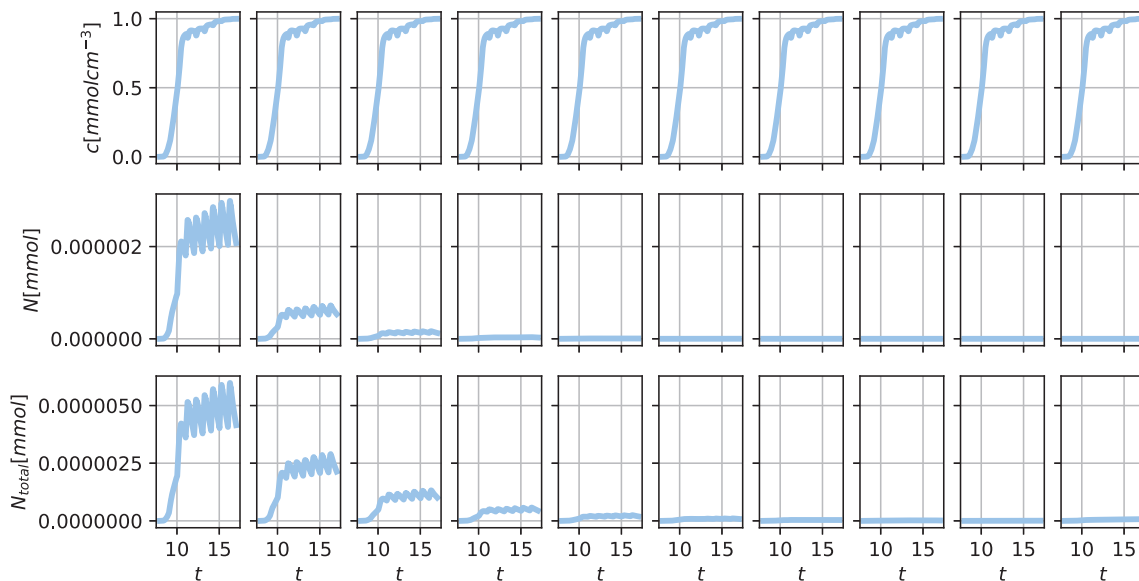


FIGURE 16 Transport in the compartments of a 0D tree. Top: volumetric concentration for each tree level. Middle: the amount of substance in one vessel per level. Bottom: the total amount of substance in all  $2^k$  vessels of the  $k$ th level in one tree.

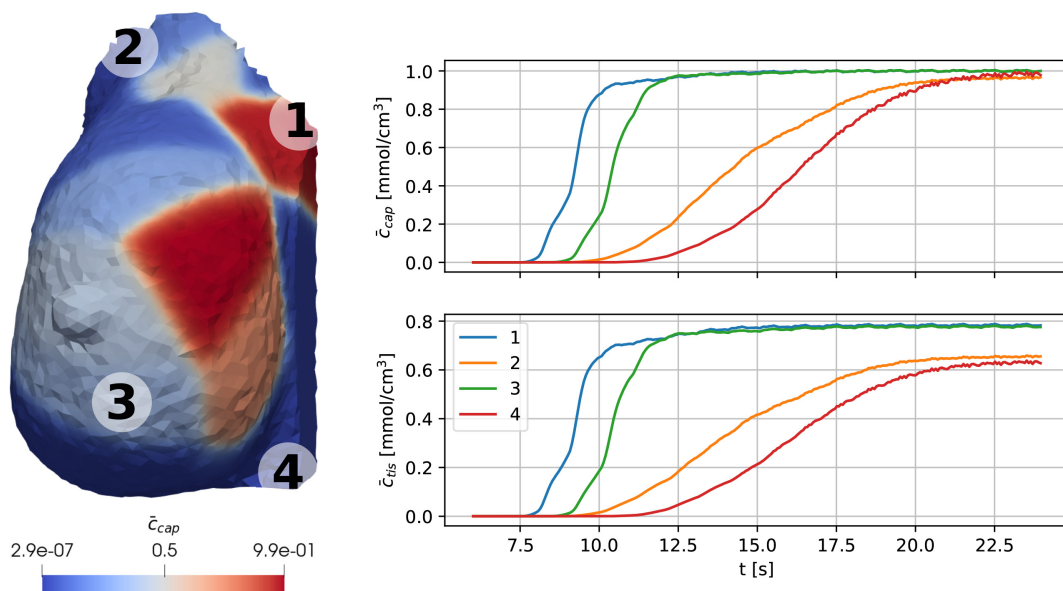
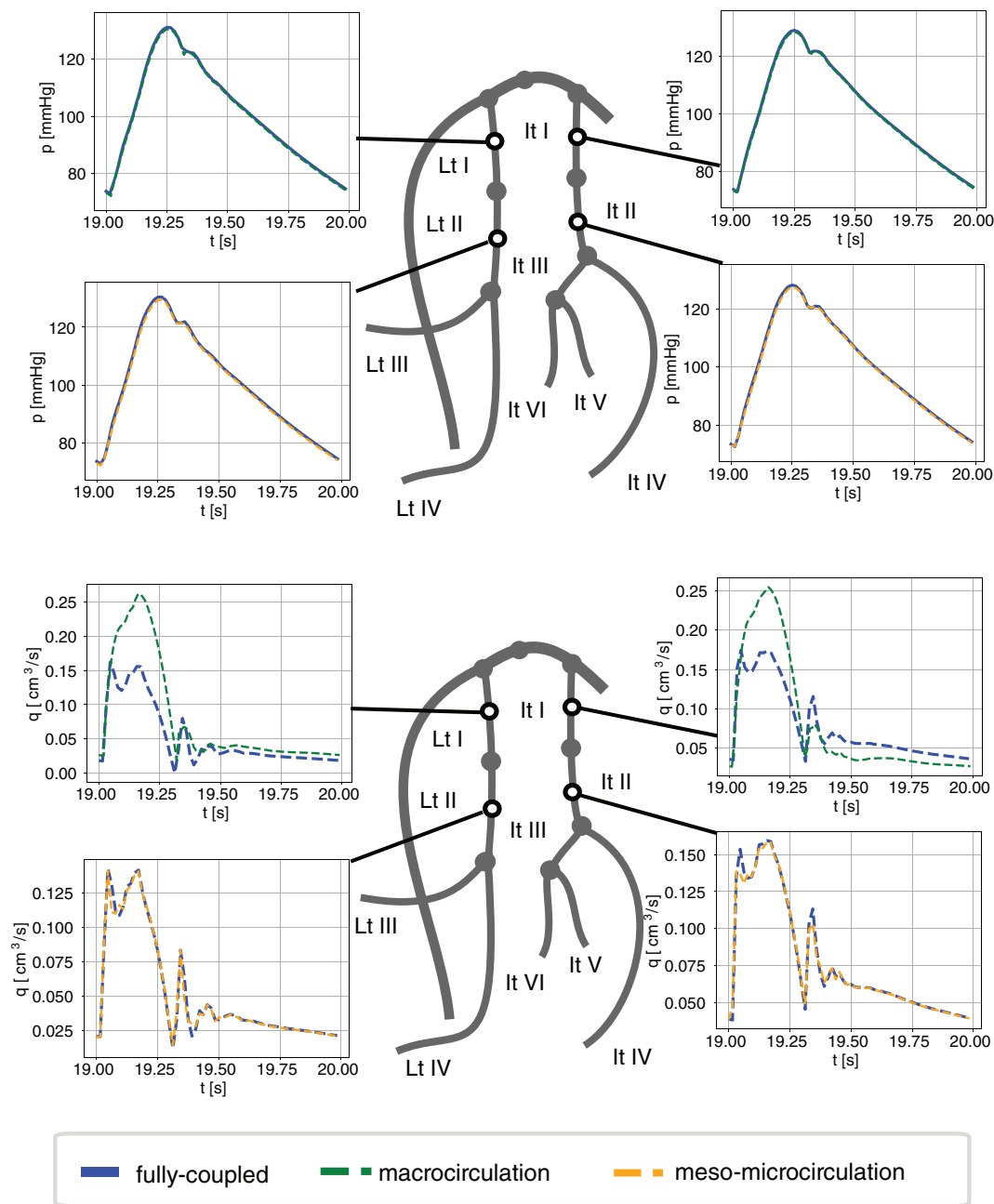
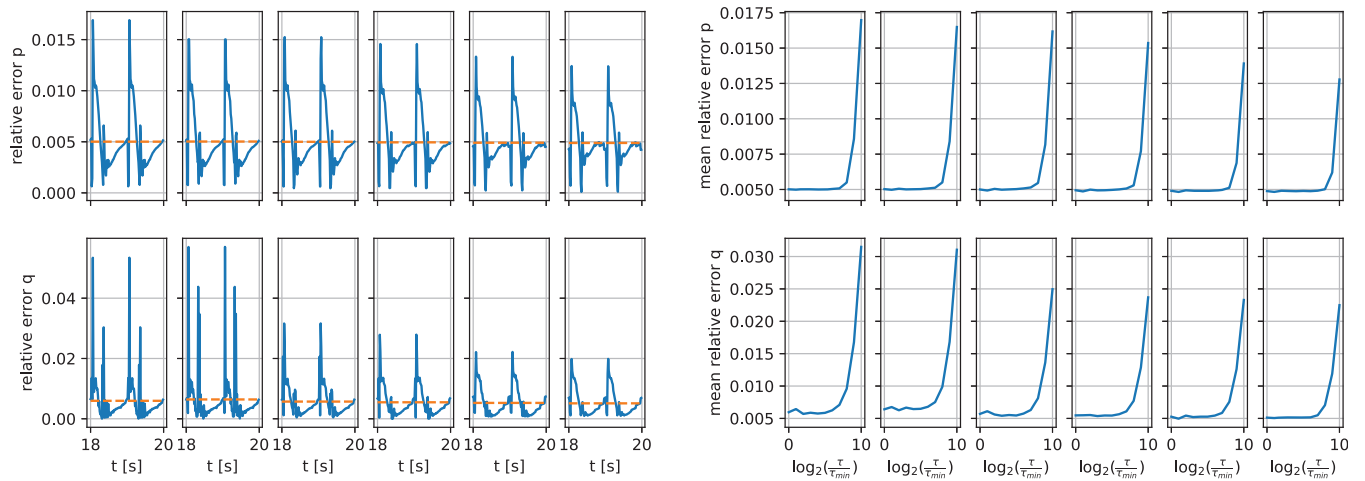


FIGURE 17 Left: concentration in capillaries at  $t = 10$ . Right: average concentrations in capillaries (upper) and tissue (lower) for the four perfusion zones marked on the left.



**FIGURE 18** Comparison between the fully coupled model and the meso-microcirculation model in the artificial extensions for the pressures and flow rates.

agreement. For the flow, the situation is significantly different. For Lt I and It I, the macrocirculation model with the Windkessel boundary overestimates the flow rate by  $\approx 30\%$  and expects more fluid to enter the breast. However for Lt II and It II, the flow rates obtained from the pressure boundary condition coincide again. Figure 19 (left) depicts the time-dependent relative error between the fully coupled and breast model along a given path for a fixed time step width  $\tau_{\min}$ . Its mean in time, depicted with a dashed line, is smaller than 1% for both the pressure and the flow. The error itself is periodic and has peaks when the underlying pressure and flow curves change in a nonsmooth way. In space, these peaks are damped, while the mean relative error stays constant. For the fully coupled model, the time step size cannot be increased due to the CFL condition of the explicit nonlinear parts in our 1D equations. This is not the case for the linearized equations for which we use an implicit scheme and can choose  $\tau$  without any restriction. Figure 19 (right) depicts the mean error between the fully coupled model at a fixed time step width  $\tau_{\min}$  versus the breast model with varying  $\tau$ . For a large range of  $\tau$ , the modeling error dominates. Thus, even increasing  $\tau$  by a factor of 100 does not



**FIGURE 19** Left: comparison between fully coupled and breast model for vessels along the path of Figure 12 (left). A solid line is used for the relative error, its mean in time is depicted with a dashed line. Right: the mean relative errors between the fully coupled model at a fixed time step  $\tau_{\min} = 1.5625 \times 10^{-5}$  s versus the breast model with a varying time step width  $\tau$ .

change the relative error. For larger  $\tau$  the error increases first in the vessels near the inlets. If we are only interested in the flow at the outlets, this justifies even more the usage of larger time step sizes.

### 7.3 | Comparison of two breast geometries

To test the robustness of our approach, we apply the breast model to a second breast geometry and compare the results of our flow model. The geometry is depicted in Figure 20A), where the inlet are marked with circles and the outlets with triangles. Just as in the previous subsections, the vessel network is connected to the Circle of Willis using the thoracic network shown in Figure 1.

Obtaining physiological meaningful pressures in the capillary bed, we quarter and halve the permeabilities  $L_{cv}$  and  $L_{tl}$  such that  $L_{cv} = 2.5 \times 10^{-9} \text{ Ba}^{-1} \text{ s}^{-1}$  and  $L_{tl} = 5 \times 10^{-9} \text{ Ba}^{-1} \text{ s}^{-1}$ . If we use the same parameter set as for the original geometry, some of the pressures in the capillary bed would become smaller than the coupled pressures from the venous system, and therefore, we would get a flow from the veins into the capillaries.

These parameters changes are related to the different shapes of both breasts, which can be observed in Figure 20B), and possible physiological differences in the patients due to different distribution of vessels. For instance, the second breast geometry has much less imaging-visible vessels in the anterior region of breast. Therefore, each terminal 1D vessel of the breast network and its attached 0D arterioles have to supply a larger region of the 3D capillary bed. These effects decrease the source parameter  $L_{ca}$  which is estimated by Equation 12 from  $L_{ca}^{(\text{breast } 1)} = 1.1 \times 10^{-6} \text{ Ba}^{-1} \text{ s}^{-1}$  to  $L_{ca}^{(\text{breast } 2)} = 3.7 \times 10^{-7} \text{ Ba}^{-1} \text{ s}^{-1}$  by 35%. This means, that we also have to rescale the sink terms modeled by  $L_{tl}$  and  $L_{cv}$ , since otherwise too much fluid volume is transferred to the lymphatic system and veins. For our workflow, this means that a calibration run for these two patient specific parameters is needed, before we can run the full patient-specific sub-model including the transport. We stress that the parameters of our generic part in the fully coupled model do not require recalibration. Moreover from the generic model, we obtain reasonable inflow information to the patient-specific submodels. For our simulations, we use a time step size of  $\tau = 2^{-11}$  s which according to Figure 19 yields accurate enough results.

In Figure 21, we show the pressures and flows for a path through the network and its attached 0D model. Inside the network the pressures are 125/70 mmHg near the inlet from the extension to 70/50 mmHg closer to the attached 0D model. The 0D model damps down the pressure amplitude further such that the final pressure at the tips of our tree is almost constant before we couple it with the homogenized capillary bed. Figure 22 shows the averaged pressures of the capillary bed and the interstitial space for each compartment  $\Omega_i$  with a unique color. The pressures of the capillaries range from 28 to 13 mmHg and they are consistently above the 10 mmHg which we assume for the venes. The amplitudes are always below 1 mmHg. For the interstitial space we get pressures from 22.5 to 10.3 mmHg.

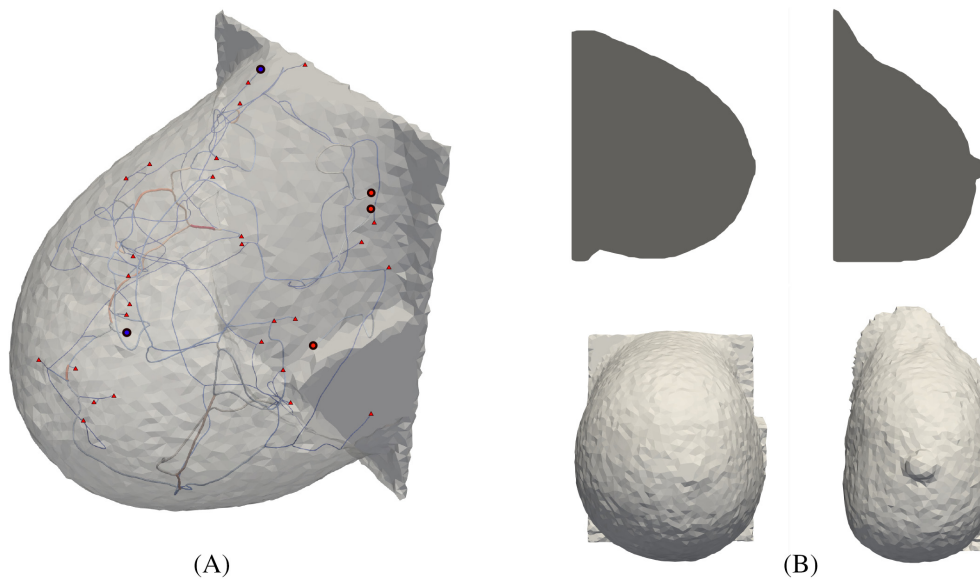


**FIGURE 20** Left: the second breast geometry including the 1D vasculature. The inlets are marked with circles and the outlets with triangles. Right: side by side comparison of the second (left) and first breast geometry (right).

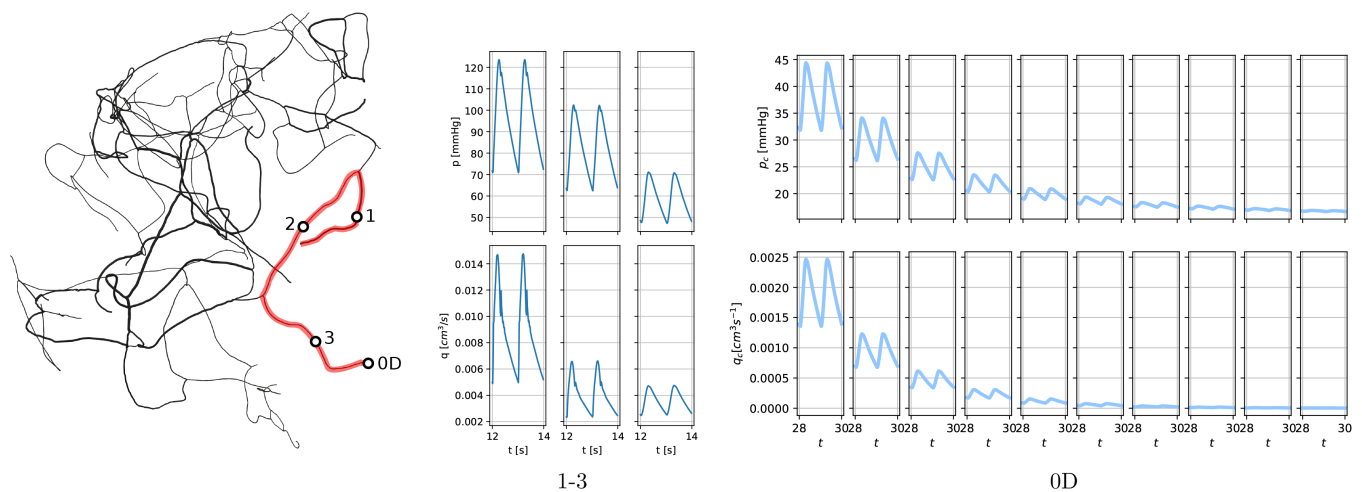


**FIGURE 21** Pressures and flows through one exemplary path in the breast geometry and in the attached 0D model.

## 7.4 | Runtime comparison flow models

In this section, we want to strengthen our claim, that the breast model can yield a significant speed up for our flow problem. Obviously, all the runtimes strongly depend on the linear solvers and on the discretizations of the different parts of our flow model. We want to stress that these results are not definitive and only serve the purpose to give an impression into the possible difference in the runtimes of the algorithms. Each component of the algorithms could be further optimized which would possibly yield significantly different results. In Figure 23, we show a runtime comparison between the different submodels. The runtimes were measured for a single processor and consisted of 100 time steps each. On the left, we show the relative runtime of one iteration of the linearized 1D model compared to one iteration of the nonlinear model for different time step widths  $\tau$ . For  $\tau = 2^{-16}$  s the relative runtime of the linearized model is approximately 1.2 and increases to 20 for  $\tau = 2^{-3}$  s. This moderate increase is due to the fact that our linear solver is not completely robust with respect to  $\tau$ . Even though each iteration takes longer, we still expect to save computational time with the breast sub-model, since significantly less iterations are needed to simulate a fixed amount of heartbeats.

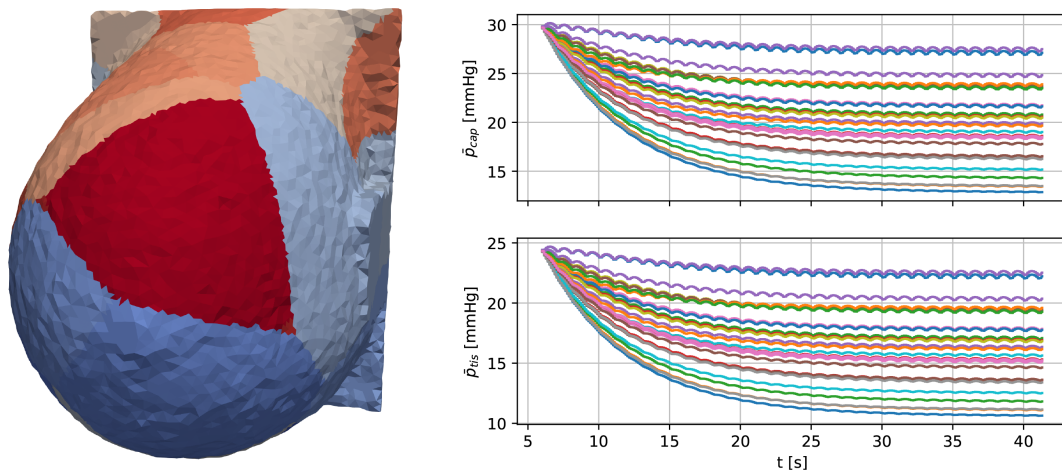


FIGURE 22 Left: perfusion zones  $\Omega_i$  of the second breast geometry. Right: averaged 3D pressures in the capillary bed and interstitial space for each perfusion zone.

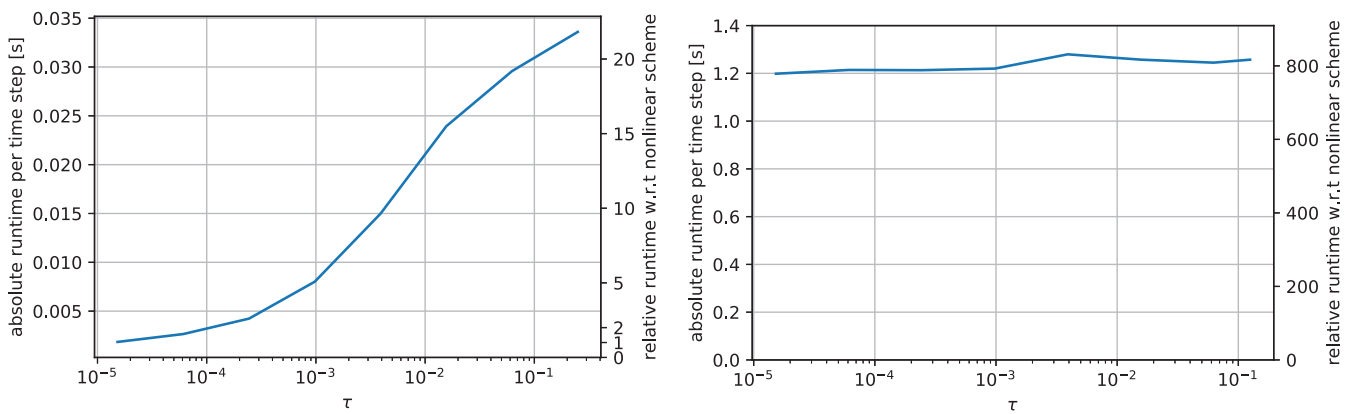


FIGURE 23 Runtime plots for the 1D-linearized flow model (left) and the 3D flow model (right) compared to the 1D-nonlinear flow model for different time step widths  $\tau$ . Left axis: the absolute runtime in seconds. Right axis: The relative runtime compared to the 1D-nonlinear flow model.

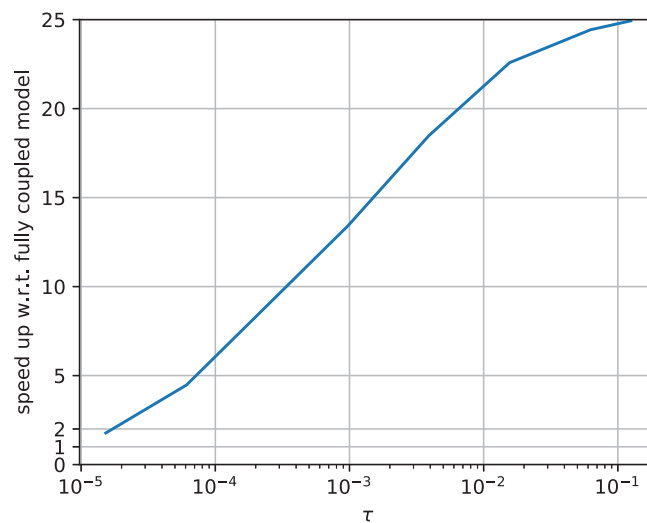


FIGURE 24 Speed up of the breast sub-model compared to the fully coupled model.

On the right, we show the runtime of one iteration of the 3D model compared to one iteration of the nonlinear model. The relative runtime of the 3D system is between 780 and 800. It slightly increases with  $\tau$ , due to a worse initial guesses for our linear solver. Note that the linear system itself is not dependent on  $\tau$ .

In Figure 24 we compare the runtime of the breast sub-model and the fully coupled model which were both simulated for one heart beat on a single processor. Using the breast model instead of the fully coupled model with the same time step size already yields a speed up of 1.8, since we circumvent the expensive calculations of the characteristics inside the nonlinear model. Increasing the time step size leads to less iterations of our 1D-0D models and hence further improves the performance, until the 3D equations start to dominate the runtime of our algorithm. The largest speed up is 25 which we attain for  $\tau = 2^{-3}$  s. From Figure 19, we can conclude that for a time step size of  $\tau = 10^{-3}$  s the solution is still accurate enough. Thus, we can expect a speed up of 10–15 by using the breast model.

## 8 | CONCLUSION AND OUTLOOK

A class of multiscale models has been introduced in this investigation to simulate flow and transport from heart to breast. To simulate the pressure amplitudes in a realistic way, a nonlinear model was used for the arteries, a linearized model for the smaller arteries, and a 0D model for the arterioles. Then this model has been coupled to the interstitial space via the homogenized 3D capillary model. Our findings are qualitatively consistent with medical knowledge about the circulation of blood within the human body. A fully coupled model has been described and compared to a simpler sub-model. It has been demonstrated experimentally that they produce sufficiently similar results for all practical purposes. The breast model consists of a nonlinear model on the patient independent parts and a linearized model for the patient specific parts. This suggests, that the expensive nonlinear computation can be done once for a large class of patients in an offline computation. For the patient specific parts, we can use a fully implicit solver allowing us to cheaply bridge long simulation times by using large time step sizes.

Results also suggest that precompiling the outlet pressures with the macrocirculation model and feeding these into the breast networks of various patients is sufficiently accurate for use in future studies of drug delivery and tumor growth. A typical example of a prevalent therapeutic procedure in which drug delivery plays a central role is systemic therapy for breast cancer patients. Thereby, a port is placed in the upper vena cava during such procedures. Chemotherapeutic drugs are injected through the port and delivered to the vasculature in the affected breast via the heart's, pulmonary circulation, and engage the larger arteries of the systemic circulation.<sup>65,66</sup> It is critical to know which portion of the injected drugs reaches the tumor in order to estimate the efficacy of this therapy. With this information, the duration rate and dose of an infusion can be optimized so that both the tumor and any negative impact of the injected drug on healthy tissue are minimized.

### ACKNOWLEDGEMENTS

This research was partially funded by the Deutsche Forschungsgemeinschaft (IGSSE, WO 671/11-1, WO 671/20-1), the U.S. Department of Energy, Office of Science, Office of Advanced Scientific Computing Research, Mathematical Multifaceted Integrated Capability Centers (Award DE-SC0019303) and the Cancer Prevention and Research Institute of Texas (CPRIT RR160005). In addition, we acknowledge the helpful feedback from our reviewers.

### FUNDING INFORMATION

DFG (IGSSE, WO 671/11-1, WO 671/20-1), U.S. Department of Energy, Office of Science, Office of Advanced Scientific Computing Research, Mathematical Multifaceted Integrated Capability Centers (Award DE-SC0019303) and Cancer Prevention and Research Institute of Texas (CPRIT RR160005).

### DATA AVAILABILITY STATEMENT

The data that support the findings of this study are openly available in Flows1D0D3D at <https://github.com/CancerModeling/Flows1D0D3D/releases/tag/v1.0>.

### ORCID

Marvin Fritz  <https://orcid.org/0000-0002-8360-7371>

Tobias Köppl  <https://orcid.org/0000-0003-3548-2807>

Andreas Wagner  <https://orcid.org/0000-0002-1622-846X>

Barbara Wohlmuth  <https://orcid.org/0000-0001-6908-6015>

Chengyue Wu  <https://orcid.org/0000-0002-3789-404X>

## REFERENCES

- D'Angelo C. Multiscale modelling of metabolism and transport phenomena in living tissues. PhD thesis. École Polytechnique Fédérale de Lausanne; 2007.
- Dewhirst M, Secomb T. Transport of drugs from blood vessels to tumour tissue. *Nat Rev Cancer*. 2017;17(12):738-750.
- Blanco PJ, Pivello M, Urquiza S, Feijóo R. On the potentialities of 3D–1D coupled models in hemodynamics simulations. *J Biomech*. 2009;42(7):919-930.
- Drziszga D, Köppl T, Pohl U, Helmig R, Wohlmuth B. Numerical modeling of compensation mechanisms for peripheral arterial stenoses. *Comput Biol Med*. 2016;70:190-201.
- El-Bouri W, Payne S. Investigating the effects of a penetrating vessel occlusion with a multi-scale microvasculature model of the human cerebral cortex. *NeuroImage*. 2018;172:94-106.
- Ho H, Sands G, Schmid H, Mithraratne K, Mallinson G, Hunter P. *A Hybrid 1D and 3D Approach to Hemodynamics Modelling for a Patient-Specific Cerebral Vasculature and Aneurysm*. Springer; 2009:323-330.
- Köppl T, Santin G, Haasdonk B, Helmig R. Numerical modelling of a peripheral arterial stenosis using dimensionally reduced models and kernel methods. *Int J Numer Methods Biomed Eng*. 2018;34(8):e3095.
- Possenti L, Gregorio DS, Gerosa F, Raimondi G, Casagrande G. A computational model for microcirculation including Fahraeus–Lindqvist effect, plasma skimming and fluid exchange with the tissue interstitium. *Int J Numer Methods Biomed Eng*. 2019;35(3):e3165.
- Józsa TI, Padmos RM, Samuels N, El-Bouri W, Hoekstra AG. A porous circulation model of the human brain for in silico clinical trials in ischaemic stroke. *Interface Focus*. 2021;11(1):20190127.
- Padmos RM, Józsa TI, El-Bouri WK, Konduri PR, Payne SJ. Coupling one-dimensional arterial blood flow to three-dimensional tissue perfusion models for in silico trials of acute ischaemic stroke. *Interface Focus*. 2021;11(1):20190125.
- Koch T, Schneider M, Helmig R, Jenny P. Modeling tissue perfusion in terms of 1d-3d embedded mixed-dimension coupled problems with distributed sources. *J Comput Phys*. 2020;410:109370.
- Wu C, Hormuth DA, Oliver TA, Pineda F, Lorenzo G. Patient-specific characterization of breast cancer hemodynamics using image-guided computational fluid dynamics. *IEEE Trans Med Imaging*. 2020;39(9):2760-2771.
- Kojic M, Milosevic M, Simic V, Koay E, Fleming J. A composite smeared finite element for mass transport in capillary systems and biological tissue. *Comput Methods Appl Mech Eng*. 2017;324:413-437.
- Hughes T, Lubliner J. On the one-dimensional theory of blood flow in the larger vessels. *Math Biosci*. 1973;18(1):161-170.
- Čanić S, Kim E. Mathematical analysis of the quasilinear effects in a hyperbolic model blood flow through compliant axi-symmetric vessels. *Math Methods Appl Sci*. 2003;26(14):1161-1186.
- Alastruey J, Parker K, Peiró J, Sherwin S. Lumped parameter outflow models for 1-D blood flow simulations: effect on pulse waves and parameter estimation. *Commun Comput Phys*. 2008;4(2):317-336.
- Stergiopoulos N, Westerhof B, Meister JJ, Westerhof N. The four-element windkessel model. Proceedings of 18th Annual International Conference of the IEEE Engineering in Medicine and Biology Society. Vol. 4. IEEE; 1996: pp. 1715–1716.
- Fernández M, Milisic V, Quarteroni A. Analysis of a geometrical multiscale blood flow model based on the coupling of ODEs and hyperbolic PDEs. *Multiscale Model Simul*. 2005;4(1):215-236.
- Rohan E, Lukeš V, Jonášová A. Modeling of the contrast-enhanced perfusion test in liver based on the multi-compartment flow in porous media. *J Math Biol*. 2018;77(2):421-454.
- Shipley RJ, Smith AF, Sweeney PW, Pries AR, Secomb TW. A hybrid discrete–continuum approach for modelling microcirculatory blood flow. *Math Med Biol: J IMA*. 2020;37(1):40-57.
- Peyrounette M, Davit Y, Quintard M, Lorthois S. Multiscale modelling of blood flow in cerebral microcirculation: details at capillary scale control accuracy at the level of the cortex. *PLoS One*. 2018;13(1):e0189474.
- Vidotto E, Koch T, Köppl T, Helmig R, Wohlmuth B. Hybrid models for simulating blood flow in microvascular networks. *Multiscale Model Simul*. 2019;17(3):1076-1102.
- Jonášová A, Rohan E, Lukeš V, Bublík O. Complex hierarchical modeling of the dynamic perfusion test: application to liver. Proceedings of the 11th World Congress on Computational Mechanics (WCCM2014), Barcelona. International Center for Numerical Methods in Engineering (CIMNE); 2014: p. 2911.
- Kremheller J, Brandstaeter S, Schrefler BA, Wall WA. Validation and parameter optimization of a hybrid embedded/homogenized solid tumor perfusion model. *Int J Numer Methods Biomed Eng*. 2021;37(8):e3508.
- Kremheller J, Vuong AT, Schrefler BA, Wall WA. An approach for vascular tumor growth based on a hybrid embedded/homogenized treatment of the vasculature within a multiphase porous medium model. *Int J Numer Methods Biomed Eng*. 2019;35(11):e3253.
- Köppl T, Wohlmuth B, Helmig R. Reduced one-dimensional modelling and numerical simulation for mass transport in fluids. *Int J Numer Methods Fluids*. 2013;72(2):135-156.
- Masri R, Puelz C, Riviere B. A reduced model for solute transport in compliant blood vessels with arbitrary axial velocity profile. *Int J Heat Mass Transf*. 2021;176:121379.
- Alastruey J, Parker K, Peiró J, Byrd S, Sherwin S. Modelling the circle of Willis to assess the effects of anatomical variations and occlusions on cerebral flows. *J Biomech*. 2007;40(8):1794-1805.

29. Barral JP, Croibier A. *Visceral Vascular Manipulations*. Churchill Livingstone; 2012.
30. Wu C, Pineda F, Hormuth DA, Karczmar GS, Yankeelov TE. Quantitative analysis of vascular properties derived from ultrafast DCE-MRI to discriminate malignant and benign breast tumors. *Magn Reson Med*. 2019;81(3):2147-2160.
31. Vignati A, Giannini V, Bert A, et al. A fully automatic multiscale 3-dimensional hessian-based algorithm for vessel detection in breast DCE-MRI. *Investig Radiol*. 2012;47(12):705-710.
32. Formaggia L, Quarteroni A, Veneziani A. *Cardiovascular Mathematics: Modelling and Simulation of the Circulatory System*. Springer; 2009.
33. Biga LM, Dawson S, Harwell A, Hopkins R, Kaufmann J. *Anatomy & Physiology*. OpenStax/Oregon State University; 2019.
34. Khaled A, Vafai K. The role of porous media in modeling flow and heat transfer in biological tissues. *Int J Heat Mass Transf*. 2003;46(26):4989-5003.
35. Støverud K, Darcis M, Helmig R, Hassanizadeh M. Modeling concentration distribution and deformation during convection-enhanced drug delivery into brain tissue. *Transp Porous Media*. 2012;92(1):119-143.
36. Obrist D, Weber B, Buck A, Jenny P. Red blood cell distribution in simplified capillary networks. *Philos Trans R Soc A Math Phys Eng Sci*. 2010;368(1921):2897-2918.
37. Secomb TW. Blood flow in the microcirculation. *Annu Rev Fluid Mech*. 2017;49:443-461.
38. Pries A, Secomb T. Rheology of the microcirculation. *Clin Hemorheol Microcirc*. 2003;29(3-4):143-148.
39. Cattaneo L. FEM for PDEs with Unfitted Interfaces: Application to Flow through Heterogeneous Media and Microcirculation. PhD thesis. Polytechnic University of Milan; 2014.
40. Erbertseder K, Reichold J, Flemisch B, Jenny P, Helmig R. A coupled discrete/continuum model for describing cancer-therapeutic transport in the lung. *PLoS One*. 2012;7(3):e31966.
41. Secomb T, Alberding J, Hsu R, Dewhirst M, Pries A. Angiogenesis: an adaptive dynamic biological patterning problem. *PLoS Comput Biol*. 2013;9(3):e1002983.
42. Pries A, Secomb T, Gaehtgens P. Biophysical aspects of blood flow in the microvasculature. *Cardiovasc Res*. 1996;32(4):654-667.
43. Formaggia L, Gerbeau JF, Nobile F, Quarteroni A. On the coupling of 3D and 1D Navier–Stokes equations for flow problems in compliant vessels. *Comput Methods Appl Mech Eng*. 2001;191(6-7):561-582.
44. Masri R, Puelz C, Riviere B. A discontinuous Galerkin method for blood flow and solute transport in one-dimensional vessel networks. *Commun Appl Math Comput*. 2022;4(2):500-529.
45. Ehlers W, Wagner A. Multi-component modelling of human brain tissue: a contribution to the constitutive and computational description of deformation, flow and diffusion processes with application to the invasive drug-delivery problem. *Comput Methods Biomech Biomed Eng*. 2015;18(8):861-879.
46. Hodneland E, Hanson E, Sevareid O, Nævdal G, Lundervold A. A new framework for assessing subject-specific whole brain circulation and perfusion using MRI-based measurements and a multi-scale continuous flow model. *PLoS Comput Biol*. 2019;15(6):e1007073.
47. Levick JR, Michel CC. Microvascular fluid exchange and the revised Starling principle. *Cardiovasc Res*. 2010;87(2):198-210.
48. Olufsen M. Structured tree outflow condition for blood flow in larger systemic arteries. *Am J Phys Heart Circ Phys*. 1999;276(1):H257-H268.
49. Fritz M, Jha PK, Köppl T, Oden JT, Wagner A. Modeling and simulation of vascular tumors embedded in evolving capillary networks. *Comput Methods Appl Mech Eng*. 2021;384:113975.
50. Köppl T, Vidotto E, Wohlmuth B. A 3D-1D coupled blood flow and oxygen transport model to generate microvascular networks. *Int J Numer Methods Biomed Eng*. 2020;36(10):e3386.
51. Murray C. The physiological principle of minimum work: I. The vascular system and the cost of blood volume. *Proc Natl Acad Sci USA*. 1926;12(3):207-214.
52. Murray C. The physiological principle of minimum work applied to the angle of branching of arteries. *J Gen Physiol*. 1926;9(6):835-841.
53. Schneider M, Reichold J, Weber B, Székely G, Hirsch S. Tissue metabolism driven arterial tree generation. *Med Image Anal*. 2012;16(7):1397-1414.
54. Schneider M, Hirsch S, Weber B, Székely G, Menze B. TGIF: Topological Gap in-Fill for Vascular Networks. International Conference on Medical Image Computing and Computer-Assisted Intervention. Springer; 2014: pp. 89–96.
55. Formaggia L, Nobile F, Quarteroni A. A one dimensional model for blood flow: application to vascular prosthesis. *Mathematical Modelling and Numerical Simulation in Continuum Mechanics*. Springer; 2002:137-153.
56. Formaggia L, Lamponi D, Quarteroni A. One-dimensional models for blood flow in arteries. *J Eng Math*. 2003;47(3):251-276.
57. Di Gregorio S, Fedele M, Pontone G, et al. A computational model applied to myocardial perfusion in the human heart: from large coronaries to microvasculature. *J Comput Phys*. 2021;424:109836.
58. Gottlieb S, Shu CW. Total variation diminishing Runge-Kutta schemes. *Math Comput*. 1996;67(221):73-85. doi:10.1090/S0025-5718-98-00913-2
59. Renard Y, Poullos K. GetFEM: automated FE modeling of multiphysics problems based on a generic weak form language. *ACM Trans Math Softw*. 2020;47(1):1-31.
60. Guennebaud G, Jacob B. Eigen v3. <http://eigen.tuxfamily.org>; 2010.
61. Balay S, Abhyankar S, Adams MF, Benson S, Brown J, PETSc/TAO users manual. Tech Rep ANL-21/39 - Revision 316, Argonne National Laboratory; 2021.

62. Kuzmin D. A vertex-based hierarchical slope limiter for p-adaptive discontinuous Galerkin methods. *J Comput Appl Math.* 2010;233(12): 3077-3085.
63. Kuzmin D. Hierarchical slope limiting in explicit and implicit discontinuous Galerkin methods. *J Comput Phys.* 2014;257:1140-1162.
64. McGuire BJ, Secomb T. Estimation of capillary density in human skeletal muscle based on maximal oxygen consumption rates. *Am J Phys Heart Circ Phys.* 2003;285(6):H2382-H2391.
65. Butros SR, Walker TG, Salazar GM, et al. Direct translumbar inferior vena cava ports for long-term central venous access in patients with cancer. *J Vasc Interv Radiol.* 2014;25(4):556-560.
66. Puel V, Caudry M, Le Métayer P, et al. Superior vena cava thrombosis related to catheter malposition in cancer chemotherapy given through implanted ports. *Cancer.* 1993;72(7):2248-2252.
67. Smith N, Pullan A, Hunter PJ. An anatomically based model of transient coronary blood flow in the heart. *SIAM J Appl Math.* 2002; 62(3):990-1018.
68. Toro EF. Brain venous haemodynamics, neurological diseases and mathematical modelling. *A Review Appl Math Comput.* 2016;272: 542-579.
69. Acosta S, Puelz C, Riviere B, Penny DJ, Rusin CG. Numerical method of characteristics for one-dimensional blood flow. *J Comput Phys.* 2015;294:96-109.
70. Puelz C, Čanić S, Rivière B, Rusin CG. Comparison of reduced models for blood flow using Runge–Kutta discontinuous Galerkin methods. *Appl Numer Math.* 2017;115:114-141.
71. Marchandise E, Willemet M, Lacroix V. A numerical hemodynamic tool for predictive vascular surgery. *Med Eng Phys.* 2009;31(1): 131-144.

**How to cite this article:** Fritz M, Köppl T, Oden JT, Wagner A, Wohlmuth B, Wu C. A 1D–0D–3D coupled model for simulating blood flow and transport processes in breast tissue. *Int J Numer Meth Biomed Engng.* 2022; 38(7):e3612. doi:[10.1002/cnm.3612](https://doi.org/10.1002/cnm.3612)

## APPENDIX A: DATA SET DESCRIPTION

The estimated parameter values for the vessels in the simulations are reported here in Table A1.

**TABLE A1** Data for the thoracic arteries as well as the breast network.

Vessel name	Id	$l$ (cm)	$r$ (cm)	$h$ (cm)	$E$ (MPa)
Subclavian artery (I)	7	1.70	0.423	0.067	0.4
Subclavian artery (II)	34	1.70	0.423	0.067	0.4
Brachial artery (I)	15	40.5	0.403	0.067	0.4
Brachial artery (II)	35	1.70	0.403	0.067	0.4
Internal thoracic artery (I)	36	2.5	0.06	0.005	1.3
Internal thoracic artery (II)	37	2.5	0.06	0.005	1.3
Internal thoracic artery (III)	38	2.0	0.06	0.005	1.3
Internal thoracic artery (IV)	39	0.5	0.06	0.005	1.3
Internal thoracic artery (V)	40	0.5	0.06	0.005	1.3
Internal thoracic artery (VI)	41	5.0	0.06	0.005	1.3
Lateral thoracic artery (I)	42	2.5	0.06	0.005	1.3
Lateral thoracic artery (II)	43	2.5	0.06	0.005	1.3
Lateral thoracic artery (III)	44	2.5	0.06	0.005	1.3
Lateral thoracic artery (IV)	45	7.0	0.06	0.005	1.3
Breast network	–	–	0.013–0.042	0.005	1.3

*Note:* The elasticity parameters and radii of the thoracic arteries are estimated. In the case of the breast network, only the wall thickness  $h$  and the elasticity  $E$  are relevant, since the lengths and radii are given by the data set from 12. For simplicity, we use for each vessel in the breast network the same wall thickness and the elasticity parameter.

## APPENDIX B: VISCOSITY

Red blood cells govern the viscosity of blood, significantly. As the red blood cells have to deform such that they can move through capillaries, the viscosity varies within the microvascular network. A quantitative relationship between the vessel diameter  $D$  is given by the following formula for the in vivo viscosity  $\mu_{bl}$  (Pa s), see<sup>42</sup>:

$$\mu_{bl}(D) = \mu_p \left( 1 + (\mu_{0.45} - 1) \frac{(1-H)^C - 1}{(1-0.45)^C - 1} \times \left( \frac{D}{D-1.1} \right)^2 \right) \times \left( \frac{D}{D-1.1} \right)^2. \quad (B1)$$

In (B1), the diameter  $D$  is dimensionless. The physical diameter  $d$  ( $\mu\text{m}$ ) has to be divided by  $1.0 \mu\text{m}$  to obtain  $D$ . Here,  $\mu_p$  (Pa s) denotes the viscosity of blood plasma, and  $H$  stands for the discharge hematocrit, which is defined by the ratio between the volume of the red blood cells and the total blood volume. The apparent viscosity  $\mu_{0.45}$  is given by:

$$\mu_{0.45} = 6.0 \exp(-0.085 \times D) + 3.2 - 2.44 \exp(-0.06 \times D^{0.645}),$$

and  $C$  is a coefficient determining the influence of  $H$  on  $\mu_{bl}$ :

$$C = (0.8 + \exp(-0.075 \times D)) \left( -1 + \frac{1}{1 + 10^{-11} D^{12}} \right) + \frac{1}{1 + 10^{-11} D^{12}}.$$

In this context, one should be aware of the fact that the constitutive relationship (B1) is known to hold for human blood.

## APPENDIX C: REDUCED 1D AND 0D MODELS

The multiscale model developed here uses various well-established submodules, which are summarized here for convenience. The reduced 1-dimensional nonlinear model and its linearized variant are given in Sections Appendix C.1 and Appendix C.2, followed by the lumped 0D Windkessel model in Section Appendix C.3.

### C.1. | Nonlinear 1D model

First, the most accurate 1D model, which consists of a set of nonlinear equations, is considered. Consider a single vessel  $\Omega_i$ ,  $i \in I_{\text{non}}$  with a length of  $l_i$ . We use a one-dimensional model to describe the propagation of pressure waves and solutes. For each curve parameter  $z \in [0, l_i]$  and a time point  $t > 0$ , we consider the section area  $A_i(z, t)$  ( $\text{cm}^2$ ), flow rate  $Q_i(z, t)$  ( $\text{cm}^3/\text{s}$ ) and averaged concentration  $\Gamma_i(z, t)$  ( $\text{mmol}/\text{cm}$ ). Averaging the Navier–Stokes equations and a convection diffusion equation across the section area and using (A1), one obtains a first order PDE-system governing  $A_i$ ,  $Q_i$  and  $\Gamma_i$ , see<sup>1,14,15</sup>:

$$\frac{\partial A_i}{\partial t} + \frac{\partial Q_i}{\partial z} = 0, \quad z \in (0, l_i), \quad t > 0, \quad (\text{C1})$$

$$\frac{\partial Q_i}{\partial t} + \frac{\partial}{\partial z} \left( \frac{Q_i^2}{A_i} \right) + \frac{A_i}{\varrho} \frac{\partial P_i}{\partial z} + 2 \times (\gamma + 2) \times \frac{\mu(2 \times R_i)}{\varrho} \times \frac{Q_i}{A_i} = 0, \quad z \in (0, l_i), \quad t > 0, \quad (\text{C2})$$

$$\frac{\partial \Gamma_i}{\partial t} + \frac{\partial}{\partial z} \left( \frac{Q_i}{A_i} \Gamma_i \right) = 0, \quad z \in (0, l_i), \quad t > 0. \quad (\text{C3})$$

Here,  $\varrho$  ( $\text{g}/\text{cm}^3$ ) is the density of blood. Since blood is assumed to be incompressible,  $\varrho$  is taken to be constant. The viscosity of blood  $\mu$  is given by (B1),  $R_i$  (cm) is the radius of the vessel  $\Omega_i$ . The choice of the dimensionless parameter  $\gamma$  depends on the type of flow and the radial velocity profile. According to Chapter 2 in [15] and Section 6.1 of [1]  $\gamma = 9$  is an appropriate choice for a turbulent flow.<sup>67</sup>  $P_i$  (Ba) denotes the fluid pressure on the vessel surface. To complete the system, we present a simple FSI-model that relates the section area  $A_i$  and the pressure  $P_i$ . The FSI model can be derived from the Young Laplace equation<sup>48,68</sup>:

$$P_i(z, t) = G_{0,i} \left( \sqrt{\frac{A_i}{A_{0,i}}} - 1 \right), \quad G_{0,i} = \frac{\sqrt{\pi} \times h_{0,i} \times E_i}{(1 - \nu^2) \times \sqrt{A_{0,i}}}, \quad (\text{C4})$$

where  $E_i$  is the Young modulus,  $A_{0,i}$  stands for the section area at rest,  $h_{0,i}$  is the vessel thickness and  $\nu$  is the Poisson ratio. Due to the fact that biological tissue is practically incompressible,  $\nu$  is chosen as  $\nu = 0.5$  (32, Chapter 10). Equation (C4) is based on the assumption that the vessel wall is instantaneously in equilibrium with the forces acting on it.

Analyzing the characteristics of this system of Equations (C1)–(C3), it can be shown that changes in pressure, flow rate, and the concentration variable are propagated by  $W_{1,i}$ ,  $W_{2,i}$  and  $W_{3,i}$ :

$$W_{1,i} = -\frac{Q_i}{A_i} + 4 \sqrt{\frac{G_{0,i}}{2\varrho}} \left( \left( \frac{A_i}{A_{0,i}} \right)^{\frac{1}{4}} - 1 \right) = -v_i + 4 \cdot (c(A_i) - c(A_{0,i})), \quad (\text{C5})$$

$$W_{2,i} = \frac{Q_i}{A_i} + 4 \sqrt{\frac{G_{0,i}}{2\varrho}} \left( \left( \frac{A_i}{A_{0,i}} \right)^{\frac{1}{4}} - 1 \right) = v_i + 4 \cdot (c(A_i) - c(A_{0,i})), \quad (\text{C6})$$

$$W_{3,i} = \frac{\Gamma_i}{A_i}. \quad (\text{C7})$$

$v_i$  (cm/s) is the flow velocity in  $\Omega_i$  and  $c(A_i)$  (cm/s) is the characteristic wave speed in  $\Omega_i$ . According to Reference [69] it can be shown that assuming  $v_i \ll c(A_i)$ , the PDE-system Equations (C1), (C2) is strictly hyperbolic. Furthermore, it is revealed that  $W_{1,i}$  can be compared to a wave moving in a negative direction and that  $W_{2,i}$  is a wave moving in a positive direction. The flow direction of  $W_{3,i}$  depends on the sign of the velocity field  $v_i$ . This information is crucial to couple the single vessels and impose boundary conditions in a consistent manner.

A branching point is referred to as  $n$ -furcation, if  $n$  vessels are coupled at this branching point. In order to couple  $n$  vessels at a branching point, we require  $3n$  equations to determine the boundary conditions for the adjacent vessels. For deriving these equations, we follow the considerations, presented in References [26,43,44]. Therefore, an index set of the vessels connected at branching point is introduced:

$$I_B = \{j_1, \dots, j_n\} \subset I_{\text{non}}.$$

The curve parameters of the corresponding inlets and outlets are denoted by  $z_{ij} \in \{0, l_{ij}\}$ . One coupling condition is motivated by enforcing mass conservation at the branching point. To achieve this, we demand that the flow rates times the ‘‘outer normal’’  $\sigma$  sum up to zero:

$$\sum_{k \in I_B} \sigma(z_k) Q_k(z_k, t) = 0, \quad \sigma(z_k) = \begin{cases} 1, & \text{if } z_k = l_k, \\ -1, & \text{if } z_k = 0. \end{cases} \quad (\text{C8})$$

Further coupling conditions are based on the continuity of the total pressure:

$$p_{t,j_1}(z_{j_1}, t) = p_{t,k}(z_k, t), \quad p_{t,k} = \frac{1}{2} \times \rho \times \left( \frac{Q_k(z_k, t)}{A_k(z_k, t)} \right)^2 + p_k(z_k, t), \quad k \in I_B \setminus \{j_1\}. \quad (\text{C9})$$

In Reference [43] it is shown that the total energy of the system is bounded by boundary conditions and initial conditions, if the continuity of the total pressure is enforced. From (C8) and (C9), we obtain  $n$  coupling conditions. Thus,  $n$  further coupling conditions are required to determine the fluid variables  $A_k(z_k, t)$  and  $Q_k(z_k, t)$ . As we know from our characteristic analysis, either  $W_{1,k}(z_k, t)$  or  $W_{2,k}(z_k, t)$  is moving towards the branching point. With  $n$  characteristic variables moving towards the  $n$ -furcation,  $n$  additional coupling conditions can be established. This results in a non-linear system of equations that has to be solved for time points of interest. A more detailed description of the system of equations can be found in References [56, 70].

For modeling transport processes through a branching point, we require some further notation. The index set  $I_B$  is divided into two disjunctive sets  $I_{B_{\text{in}}}$  and  $I_{B_{\text{out}}}$ . For these index sets it holds:

$$k \in I_{B_{\text{in}}} \Leftrightarrow (z_k = 0 \wedge Q_k(z_k, t) \leq 0) \vee (z_k = l_k \wedge Q_k(z_k, t) \geq 0),$$

and

$$k \in I_{B_{\text{out}}} \Leftrightarrow (z_k = 0 \wedge Q_k(z_k, t) > 0) \vee (z_k = l_k \wedge Q_k(z_k, t) < 0).$$

Accordingly, the conservation of solute mass at a branching point can be formulated as follows:

$$N_{\text{in}}(t) = \sum_{k \in I_{B_{\text{in}}}} |Q_k(z_k, t)| \frac{\Gamma_k(z_k, t)}{A_k(z_k, t)} = \sum_{k \in I_{B_{\text{out}}}} |Q_k(z_k, t)| \frac{\Gamma_k(z_k, t)}{A_k(z_k, t)}. \quad (\text{C10})$$

$N_{\text{in}}$  (mmol/s) is the number of particles flowing through the bifurcation within a second. Next, we note that the concentration variables  $\Gamma_k(z_k, t)$ ,  $k \in I_{B_{\text{in}}}$  can be determined by means of an upwinding method, since the

corresponding characteristic variables  $W_3(z_k, t)$  are leaving the inflow vessels and entering the bifurcation. This means that  $N_{in}$  can be computed for each time point  $t > 0$ . It remains to determine  $\Gamma_k(z_k, t)$ ,  $k \in I_{B_{out}}$ . For this purpose, we assume that an instantaneous mixing at the branching point takes place. This means that:

$$\frac{\Gamma_k(z_k, t)}{A_k(z_k, t)} = W_{3,k}(z_k, t) \equiv \text{constant}, \quad \forall k \in I_{B_{out}}.$$

Taking this into account and using the mass conservation for the fluid system, it holds for  $l \in I_{B_{out}}$ :

$$\Gamma_l(z_l, t) = \frac{A_l(z_l, t)}{|Q_l(z_k, t)|} \times N_{in}(t) \times \frac{|Q_l(z_k, t)|}{\sum_{k \in I_{B_{in}}} |Q_k(z_k, t)|} = \frac{A_l(z_l, t) \times N_{in}(t)}{\sum_{k \in I_{B_{in}}} |Q_k(z_k, t)|}. \quad (\text{C11})$$

This completes the coupling conditions of the nonlinear scheme.

## C.2. | Linearized 1D model

After introducing the nonlinear model, we move one step further down the vascular tree and consider smaller vessels for which a linearized equation is sufficient. To a vessel  $\Omega_i$ ,  $i \in I_{lin}$  of length  $l_i$ , we assign a pressure variable  $p_i$  (Ba), a flow rate  $q_i$  (cm<sup>3</sup>/s) and the averaged concentration variable  $\Gamma_i$  (mmol/cm). Based on assumption (A2), 1D linearized version of (C1)–(C3) is used to model flow and transport within the breast network. Its derivation is based on the assumption  $A_i \approx A_{i,0}$  and can be found in Section 6.2.1 of Reference [1]:

$$\frac{\partial p_i}{\partial t} + \frac{1}{\tilde{C}_i} \frac{\partial q_i}{\partial z} = 0, \quad z \in (0, l_i), \quad t > 0, \quad (\text{C12})$$

$$\frac{\partial q_i}{\partial t} + \frac{1}{L_i} \frac{\partial p_i}{\partial z} + K_{r,i} \times \frac{q_i}{A_{0,i}} = 0, \quad z \in (0, l_i), \quad t > 0, \quad (\text{C13})$$

$$\frac{\partial \Gamma_i}{\partial t} + \frac{\partial}{\partial z} \left( \frac{q_i}{A_{0,i} + \tilde{C}_i p_i} \Gamma_i \right) = 0, \quad z \in (0, l_i), \quad t > 0. \quad (\text{C14})$$

The parameters  $\tilde{C}_i$ ,  $L_i$  and  $k_{r,i}$  represent the wall compliance, inertia and resistance parameter of vessel  $\Omega_i$ , they are given by:

$$\tilde{C}_i = \frac{A_{0,i}}{q \cdot c(A_{0,i})}, \quad L_i = \frac{q}{A_{0,i}}, \quad K_{r,i} = 2 \times (\gamma + 2) \times \frac{\mu(2 \times R_{0,i})}{q}.$$

Here,  $R_{0,i}$  (cm) is the radius of vessel  $\Omega_i$ . It is given by  $R_{0,i} = \sqrt{A_{0,i}/\pi}$ . Since we assumed laminar and Poiseuille type flow, the parameter  $\gamma$  is set to two according to Section 6.1 of 1. Again the viscosity parameter  $\mu$  is given by (B1) to account for non-Newtonian effects.

Similar to (C1)–(C3) one can show that the first order PDE-system (C12)–(C14) is hyperbolic and that the solution variables can be transformed into characteristic variables  $w_{1,i}$ ,  $w_{2,i}$  and  $w_{3,i}$ . The first two characteristic variables are connected to the fluid variables  $p_i$  and  $q_i$ , and  $w_{3,i}$  is related to  $\Gamma_i$ :

$$w_{1,i} = \frac{1}{2} \left( -\sqrt{\frac{\tilde{C}_i}{L_i}} p_i + q_i \right), \quad w_{2,i} = \frac{1}{2} \left( \sqrt{\frac{\tilde{C}_i}{L_i}} p_i + q_i \right) \quad \text{and} \quad w_{3,i} = \frac{\Gamma_i}{A_{0,i} + \tilde{C}_i p_i}. \quad (\text{C15})$$

Thereby,  $w_{1,i}$  can be compared to a wave moving into negative direction, while  $w_{2,i}$  is moving in the opposite direction. The direction of motion of  $w_{3,i}$  depends on the sign of  $q_i$ . As for the non-linear PDE-system (C1)–(C3) this knowledge is important to impose boundary conditions in a meaningful manner.

Coupling  $n$  linear flow and transport models (C12)–(C14) at a branching point can be done in a similar way as in the non-linear case. Replacing in (C8)  $Q_k$  by  $q_k$ , we obtain the mass conservation equation. The continuity of the total pressure is replaced by the continuity of the fluid pressure [1]:

$$p_{j_1}(z_{j_1}, t) = p_k(z_k, t), \quad k \in I_B \setminus \{j_1\}.$$

Closing the system, the outgoing characteristic variables are extrapolated using (C15). This yields a linear system of equations governing the fluid variables at a branching point. The concentration variables are determined similar to (C10). Replacing  $Q_k$  by  $q_k$  and  $A_l$  by  $A_{0,l}$  in (C10) the concentration values for the vessels in  $I_{B_{out}}$  are obtained. The concentration values for the vessels in  $I_{B_{in}}$  are obtained by extrapolating the outgoing characteristics.

### C.3. | 0D Windkessel model

We consider a vessel  $\Omega_i$  with  $i \in I_{wk}$  and assume that their parametrization is oriented such that  $z_i = l_i$  is adjacent to the outlets. At the outlet of a larger artery  $\Omega_i$ , the reflections of the pulse waves at the omitted vessels have to be incorporated to be able to simulate realistic pressure and velocity curves. For this purpose, we assign to each terminal vessel a reflection parameter  $R_{p,i} = R_{1,i} + R_{2,i}$ , where  $R_{1,i}$  is the resistance parameter of  $\Omega_i$  [16]:

$$R_{1,i} = \frac{\rho \times c(A_{0,i})}{A_{0,i}}.$$

This choice is motivated by the goal to keep the artificial reflection at the interface between the 1D and the 0D model at a minimum.  $R_{2,i}$  is the resistance parameter for all the vessels that are connected to  $\Omega_i$  but not contained in the macrocirculation. The third parameter  $C_i$  represents the compliance of the omitted vessels and is a measure of the ability of these vessels to store a certain blood volume. The triple  $(R_{1,i}, C_i, R_{2,i})$  is referred to as a “three-element Windkessel” model in [16,32]. The values for the Windkessel parameters used in our simulations are listed in Table 1 of [28]. In order to describe the dynamics of a Windkessel model, the following ODE has been derived using averaging techniques and an analogy from electrical science [16,28,71]:

$$C_i \frac{dp_{c,i}}{dt} = \frac{P_i(l_i, t) - p_{c,i}}{R_{1,i}} - \frac{p_{c,i} - p_v}{R_{2,i}}, \quad (C16)$$

$$Q_i(l_i, t) = \frac{P_i(l_i, t) - p_{c,i}}{R_{1,i}}, \quad Q_{ven,i} = \frac{p_{c,i} - p_v}{R_{2,i}}.$$

$P_i(l_i, t) = p_i(A_i(l_i, t))$  is given by (C4). Here,  $p_{c,i}$  and  $p_v$  are averaged arterial and venous pressures and  $Q_{ven,i}$  represents the flow rate from the arterial system into the venous system. Solving (C16) and using the outgoing characteristic variable  $W_{2,i}(l_i, t)$ , the boundary conditions for  $A_i(l_i, t)$  and  $Q_i(l_i, t)$  can be determined. Further details can be found, for example, in [16,28,71]. It remains to model the behavior of the concentration variable at an outlet.

For  $\Gamma_i(l_i, t)$ , a concentration variable  $c_i$  (mmol/cm<sup>3</sup>) is introduced for the omitted arterial system and to establish a mass balance equation for the solute particles leaving or entering the omitted arterial system:

$$\frac{d}{dt}(V_i(t)c_i(t)) = N_i(t) - N_{ven}(t),$$

where  $N_i$  (mmol/s) represents the number of particles leaving or entering the terminal 1D vessel per second, while  $N_{\text{ven}}$  (mmol/s) denotes the number of particles migrating into the venous system during a second. Moreover,  $V_i$  (cm<sup>3</sup>) is the fluid volume contained in the omitted arterial system. It can be computed by means of the following ODE:

$$\frac{dV_i}{dt} = Q_i(l_i, t) - Q_{\text{ven},i}(t). \quad (\text{C17})$$

To determine  $N_i$ , we have to check the sign of  $Q_i(l_i, t)$ :

$$N_i(t) = \begin{cases} \frac{\Gamma_i(l_i, t)Q_i(l_i, t)}{A_i(l_i, t)}, & \text{if } Q_i(l_i, t) \geq 0, \\ Q_i(l_i, t) \cdot c_i(t), & \text{if } Q_i(l_i, t) < 0. \end{cases}$$

Assuming that  $Q_{\text{ven},i} \geq 0$ ,  $N_{\text{ven}}(t)$  is given by:

$$N_{\text{ven}}(t) = c_i(t) \times Q_{\text{ven},i}(t) = c_i(t) \times \frac{P_{c,i} - P_v}{R_{2,i}}.$$

Summarizing the above equations, the following ODE for  $c_i$  results:

$$\frac{d}{dt}(V_i(t)c_i(t)) = \begin{cases} \frac{\Gamma_i(l_i, t)Q_i(l_i, t)}{A_i(l_i, t)} - c_i(t) \times \frac{P_{c,i} - P_v}{R_{2,i}}, & \text{if } Q_i(l_i, t) \geq 0, \\ Q_i(l_i, t) \cdot c_i(t) - c_i(t) \times \frac{P_{c,i} - P_v}{R_{2,i}}, & \text{if } Q_i(l_i, t) < 0. \end{cases} \quad (\text{C18})$$

Solving (C17) and (C18) for each time point, we have for  $\Gamma_i(l_i, t)$ :

$$\Gamma_i(l_i, t) = \begin{cases} W_{3,i}(l_i, t) \times A_i(l_i, t), & \text{if } Q_i(l_i, t) \geq 0, \\ c_i(t) \times A_i(l_i, t), & \text{if } Q_i(l_i, t) < 0. \end{cases} \quad (\text{C19})$$